AMI observations of ten CLASH galaxy clusters: SZ and X-ray data used together to determine cluster dynamical states

Clare Rumsey,[1][*] Malak Olamaie[1], Yvette C. Perrott[1], Helen R. Russell[3]
Farhan Feroz[1], Keith J. B. Grainge[4,1], Will J. Handley[1,2], Michael P. Hobson[1],
Richard D. E. Saunders[1,2], Michel P. Schammel[1]

[1] *Astrophysics Group, Cavendish Laboratory, 19 J. J. Thomson Avenue, Cambridge, CB3 0HE*
[2] *Kavli Institute for Cosmology Cambridge, Madingley Road,Cambridge, CB3 0HA*
[3] *Institute of Astronomy, Madingley Road, Cambridge CB3 0HA*
[4] *Jodrell Bank Centre for Astrophysics, School of Physics and Astronomy, Manchester, M13 9PL*

ABSTRACT

Using Arcminute Microkelvin Imager (AMI) SZ observations towards ten CLASH clusters we investigate the influence of cluster mergers on observational galaxy cluster studies. Although selected to be largely relaxed, there is disagreement in the literature on the dynamical states of CLASH sample members. We analyse our AMI data in a fully Bayesian way to produce estimated cluster parameters and consider the intrinsic correlations in our NFW/GNFW-based model. Varying pressure profile shape parameters, illustrating an influence of mergers on scaling relations, induces small deviations from the canonical self-similar predictions – in agreement with simulations of Poole et al. (2007) who found that merger activity causes only small scatter perpendicular to the relations. We demonstrate this effect observationally using the different dependencies of SZ and X-ray signals to n_e that cause different sensitivities to the shocking and/or fractionation produced by mergers. Plotting Y_X–M_{gas} relations (where $Y_X = M_{gas}T$) derived from AMI SZ and from *Chandra* X-ray gives ratios of AMI and *Chandra* Y_X and M_{gas} estimates that indicate movement of clusters *along* the scaling relation, as predicted by Poole et al. (2007). Clusters that have moved most along the relation have the most discrepant T_{SZ} and T_X estimates: all the other clusters (apart from one) have SZ and X-ray estimates of M_{gas}, T and Y_X that agree within r_{500}. We use SZ vs X-ray discrepancies in conjunction with *Chandra* maps and T_X profiles, making comparisons with simulated cluster merger maps in Poole et al. (2006), to identify disturbed members of our sample and estimate merger stages.

Key words: galaxies: clusters: general – methods: observational – techniques: interferometric – large-scale structure of the Universe.

1 INTRODUCTION

Physical parameters of glaxy clusters, such as total mass and gas mass, are commonly studied through scaling relations. These relations assume that both growing and mature clusters are relaxed, self-similar systems such that relations between e.g. L_X, L_{SZ}, M_{tot}, M_{gas}, T, etc. are simple power laws (see e.g. Kaiser 1986 and Giodini et al. 2013 for a recent review). Deviations from hydrostatic equilibrium (HSE) (or from virialisation) and self-similarity during cluster mergers will cause scatter around the scaling relations. Studies in the literature aim to use these relations to make accurate determinations of e.g. total cluster mass, and therefore often focus on minimising the scatter either by careful sample selection of low-redshift, relaxed clusters (e.g. Zhang et al. 2008, Pratt et al. 2009, Sun et al. 2009, Vikhlinin et al. 2009a), or by finding a particularly low-scatter mass proxy (e.g. Kravtsov, Vikhlinin, & Nagai 2006, Arnaud, Pointecouteau, & Pratt 2007, Zhang et al. 2008, Mahdavi et al. 2013). These approaches often produce low-scatter relations that agree with the self-similar predictions. However, Poole et al. (2007), using simulations of two-body cluster mergers to track the evolution of a merger (from a relaxed system before the start of the merger through to relaxation of the merged system) in the plane of a scaling relation, find large changes in cluster observables *along* the relation with little perpendicular displacement.

Assessment of these cluster parameter values through calculation from Sunyaev–Zel'dovich (SZ, Sunyaev & Zel'dovich 1972)

[*] Email:cr461@mrao.cam.ac.uk

Table 1. Summary of assessments that we have found in the literature of the dynamical states of the AMI-CLASH sub-sample.

Cluster	Relaxed	Unrelaxed	Notes
A611	✓		Widely agreed relaxed, see e.g. Allen et al. (2008), Donnarumma et al. (2011)
A1423	✓	✓	Relaxed: e.g. classified 'non-distorted' by Hashimoto et al. (2007) and 'regular' by Bauer et al. (2005)
			Unrelaxed: due to centroid shift, cuspiness and cooling time – Landry et al. (2013)
A2261	✓	✓	Widely considered relaxed, see e.g. Landry et al. (2013), Mann & Ebeling (2012)
			Unrelaxed due to extra structure to the south-west, Gilmour, Best, & Almaini (2009)
CLJ1226+3332	✓	✓	Classified relaxed e.g. Maughan et al. (2004), Allen et al. (2008)
			Merger given X-ray morphology, Vikhlinin et al. (2009a), and temperature map, Maughan et al. (2007)
MAJ0647+7015		✓	Strong-lens selected, highly unrelaxed: Zitrin et al. (2013)
MAJ0717+3745		✓	Strong-lens selected, highly unrelaxed and complex merger: Medezinski et al. (2013)
MAJ0744+3927	✓	✓	In samples of large relaxed clusters Allen et al. (2004), Schmidt & Allen (2007), and Allen et al. (2008)
			Substructure identified, e.g. Schmidt & Allen (2007), Allen et al. (2008). Disturbed, Sayers et al. (2013)
MAJ1149+2223		✓	Strong-lens selected, highly complex merger, see Smith et al. (2009)
MAJ1423+2404	✓		Highly relaxed state, pronounced cool-core, e.g. Ebeling et al. (2007) and Limousin et al. (2010)
RXJ1532+3021	✓	✓	Presence of a cool-core e.g. Allen et al. (2008), Hlavacek-Larrondo et al. (2013) classifies it as relaxed
			Cold front possibly from low-level merger turbulence (Hlavacek-Larrondo et al. 2013)

and X-ray observation provides a critical probe of the dynamical state of the cluster gas due to the difference in dependencies of the SZ and X-ray flux densities on the electron number density, n_e. The SZ effect is the inverse Compton scattering of CMB photons by hot cluster gas, and is $\propto \int n_e T \, dl$, where T is the plasma temperature and dl the line element along the line of sight through the cluster. The X-ray Bremsstrahlung signal is $\propto \int n_e^2 \Lambda(T) \, dl$, where Λ is the cooling function ($\Lambda \propto T^{\frac{1}{2}}$ for the clusters in this paper). Parameter values estimated from measurement of SZ and X-ray signals will, therefore, also depend differently on n_e and T.

As cluster mergers are known to produce regions of higher density gas, through processes such as shocking, X-ray parameter estimation is likely more sensitive to dynamical state, and will produce larger displacements along scaling relations during a merger than SZ parameter values. This implies that merger activity can be identified by looking at discrepancies between SZ and X-ray measurements.

To test this observationally, we use the CLASH sample of well-studied clusters selected by Postman et al. (2012) to form a sample of massive clusters, most of which are classified in the literature as relaxed, plus a small number of clusters with pronounced strong gravitational lensing (see Section 2). Here we discuss measurements of a sub-sample of CLASH clusters via the SZ effect using the Arcminute Microkelvin Imager (AMI, Zwart et al. 2008).

The SZ signal measures the Comptonization parameter, y, the line-of-sight integral of the number of collisions multiplied by the mean fractional energy change of the CMB photons per collision:

$$y = \frac{\sigma_T}{m_e c^2} \int n_e k_B T \, dl \tag{1}$$

$$= \frac{\sigma_T}{m_e c^2} \int P_e \, dl, \tag{2}$$

where σ_T is the Thomson scattering cross-section, m_e the electron mass, c the speed of light. Equation 2 shows that the SZ surface brightness is proportional to the electron pressure, P_e, assuming

an ideal gas law, integrated along the line of sight. Integrating y over the solid angle Ω subtended by the cluster gives Y_{SZ}, which quantifies the internal energy of the cluster gas, providing a proxy for total mass, given redshift information.

In X-ray studies Y_X, found from $Y_X = M_{gas} T_X$, is used as an analogue of Y_{SZ} which is proportional to the product of the gas mass and the mean temperature measured from SZ within a sphere (or a cylinder). Kravtsov, Vikhlinin, & Nagai (2006) find, using simulated data, that Y_X provides an equally good proxy for total mass as Y_{SZ}. The mean cluster temperature has also been widely used as a proxy for total cluster mass. Cluster T has traditionally been measured through X-ray spectroscopy; with good enough sensitivity and angular resolution, annular averaging gives temperature profiles out to, for some clusters, radii of ≈ 1 Mpc (see e.g. ACCEPT Database, Cavagnolo et al. 2009, Vikhlinin et al. 2006, Pratt, Arnaud, & Pointecouteau 2006). Olamaie, Hobson, & Grainge (2012) and Olamaie, Hobson, & Grainge (2013) show that a gas temperature profile can also be obtained via SZ observation, given assumed geometry and dynamical state, and given a prior on the gas fraction f_{gas} at r_{200}.

In this study, cluster parameters are derived from our AMI SZ measurements in a fully Bayesian way using the model described in Olamaie, Hobson, & Grainge (2012) and (2013). This model uses a Navarro, Frenk and White (NFW) profile to describe the dark matter density, which is believed, from cosmological N-body simulations, to accurately model all dark matter halos (Navarro, Frenk, & White 1997). A generalised Navarro, Frenk and White (GNFW) profile is used to describe the gas pressure, shown to follow self-similarity more closely than the density or temperature at high radius (Nagai, Kravtsov, & Vikhlinin 2007). Further conditions of spherical symmetry, HSE, and a small $f_{gas, r_{200}}$ compared to unity, produces cluster properties as functions of radius.

Throughout, we assume $H_0 = 70$ km s^{-1}Mpc^{-1} and a concordance ΛCDM cosmology with $\Omega_m = 0.3$, $\Omega_\Lambda = 0.7$, $\Omega_k = 0$, $\Omega_b =$

Table 2. Summary of AMI characteristics

	SA	LA
Antenna diameter	3.7 m	12.8 m
Number of antennas	10	8
Baseline lengths (current)	5–20 m	18–110 m
Primary beam (15.7 GHz)	20.1 arcmin	5.5 arcmin
Typical synthesized beam	3 arcmin	30 arcsec
Flux sensitivity	30 mJy $s^{1/2}$	3 mJy $s^{1/2}$
Observing frequency	13.9–18.2 GHz	
Bandwidth	4.3 GHz	
Channel bandwidth	0.72 GHz	

Table 3. AMI actual observing time in hours for each cluster in the AMI-CLASH sub-sample.

Cluster	SA		LA	
	2009-12	new	2009-12	new
A611	18	16	24	14
A1423	57	–	18	8
A2261	60	8	7	124
CLJ1226+3332	77	–	48	–
MAJ0647+7015	25	8	21	8
MAJ0717+3745	49	9	30	38
MAJ0744+3927	16	9	10	8
MAJ1149+2223	38	7	18	16
MAJ1423+2404	42	7	27	8
RXJ1532+3021	63	77	25	33

0.041, $\omega_0 = -1$, $\omega_a = 0$ and $\sigma_8 = 0.8$. All cluster parameter values are at the redshift of the cluster. We emphasise that we denote $M_{gas}T$ as Y_X for either SZ or X-ray.

2 THE AMI-CLASH SUB-SAMPLE

The CLASH (Cluster Lensing and Supernova Survey with Hubble) sample consists of 25 massive clusters, covering a large redshift range (*z* from 0.213 to 0.888), selected for strong and weak lensing observation with Hubble and *Subaru* (Postman et al. 2012). 20 of these clusters were selected from *Chandra* X-ray observations to be dynamically relaxed. The remaining five clusters were selected solely based on their high lensing-strength and consequently include some of the most disturbed clusters known (Redlich et al. 2012). Eleven of these clusters are visible to AMI which is currently restricted to a declination range of 20° to 85°. Since the CLASH sample is composed mainly of Abell and MACS clusters, all eleven clusters in the sub-sample had in fact been observed (with varying sensitivities) by AMI in 2009 to 2012. These observations showed that the field of view of MAJ1720+3536 contains too bright a source to allow SZ mapping with AMI. We discard this cluster leaving an AMI-CLASH sub-sample of ten. We have searched the literature to find additional assessments of the dynamical states and X-ray morphologies of the ten clusters; Table 1 summarises these findings.

3 AMI AND OBSERVATIONS

SZ observations were carried out with AMI, a dual array of interferometers observing at centre-frequency 15.7 GHz, located near

Cambridge. The arrangement of ten 3.7-m antennas with baselines of 5–20 m in the Small Array (SA) and eight 12.8-m antennas with baselines of 18–110 m in the Large Array (LA) allows for study of the large-scale SZ effect from clusters along with subtraction of otherwise confusing radio sources. For a full description of the instrument see Zwart et al. (2008). Our pointing strategy for each cluster is as follows. A single SA pointing centre is observed, centred on the cluster X-ray centre. For the LA, the smaller primary beam size (see Table 2) requires that the same area is covered with a mosaiced 61-point LA observation; the central 19 pointings of this are observed 3× longer than the outer pointings to reach lower noise levels near the cluster centre. Our sensitivity aim for each cluster has been to achieve thermal noise levels below 100 µJy in the centre of the SA maps and averaging below 80 µJy over the central 19-pointings of the LA maps. The 2009-2012 observations of CLJ1226+3332 on both arrays and the SA 2009-2012 observations of A1423 and MAJ1423+2404 have the sensitivities that we require. For the rest we have made new observations so that these, plus the 2009-2012 observations, achieve the sensitivity aim. A summary of the observations carried out is presented in Table 3. Note that, for RXJ1532+3021, 2009-2012 observations were made with a somewhat erroneous pointing centre, and we use only new, correctly centred, observations.

Data processing is carried out with our in-house software package REDUCE, in which the raw data are calibrated and flagged for interference and telescope errors. Note that all AMI data, whenever taken, have been reduced with our latest reduction pipeline with optimised interference flagging and calibration. Flux calibration is carried out with observations of 3C 48, 3C 147 and 3C 286, with 3C 286 flux densities calibrated against Very Large Array (VLA) measurements (Perley & Butler 2013). Data are Fourier transformed into frequency channels and then written out as *uv-*FITS files. Data *uv-*FITS files from 2009-2012 and from new observations are concatenated in *uv*-space to produce a single data set in each array. For source-finding and for initial visual inspection of a cluster field, the *uv*-data are imaged in AIPS[1] using automated CLEAN procedures with noise levels determined using IMEAN. The LA channel maps are passed through the SOURCE-FIND algorithm (Franzen et al. 2011) which estimates LA source positions, flux densities and spectral indices to use as priors in McADAM (Feroz et al. 2009), our Bayesian analysis system (Section 4). If sources in the fields exhibit variability, concatenating *uv*-data taken a few years apart could introduce inaccuracies in source flux estimates between the arrays. If the proportion of old data and new data is different between the arrays, the average SA flux may be significantly different from the average LA flux that is being subtracted, leaving residuals. Only a few sources in the maps show variability between old (2009-2012) and new (2013-2014) observations at a level that would effect parameter estimation if the LA flux was directly subtracted from the SA data. This effect is accounted for in McADAM (Section 4).

4 PARAMETER ESTIMATION

Analysis of AMI data is carried out in *uv*-space using our Bayesian analysis package McADAM (Feroz et al. 2009) which uses the fast sampler MULTINEST (Feroz & Hobson 2008, Feroz, Hobson, & Bridges 2009 and Feroz et al. 2013) to estimate cluster parameters given a cluster model; McADAM simultaneously fits the radio

---

[1] http://aips.nrao.edu/

Table 4. Summary of the priors used in the analysis using the model described in Section 4.1. $M_{\mathrm{tot},r_{200}}$ and $f_{\mathrm{gas},r_{200}}$ are the total mass internal to r_{200} and gas fraction internal to r_{200}, respectively.

Parameter	Prior
Cluster position $(x_{\mathrm{c}}, y_{\mathrm{c}})$	Gaussian at SA pointing centre, σ set at 60 arcsec regardless of precision of cluster position
Mass $(M_{\mathrm{tot},r_{200}}/\mathrm{M}_\odot)$	Uniform in log space between 1×10^{14} and 6×10^{15}
Gas fraction $(f_{\mathrm{gas},r_{200}})$	Gaussian with $\mu = 0.13$, $\sigma = 0.02$
Shape parameters (a, b, c, c_{500})	Delta-function with "universal" values, see Arnaud et al. (2010)
Source position $(x_{\mathrm{s}}, y_{\mathrm{s}})$	Delta-function at LA position
Source flux density $(S_0/Jy) > 4\sigma_{\mathrm{SA}}$	Gaussian at LA value, with $\sigma = 40$ per cent of LA flux density
Source spectral index when $S_0 > 4\sigma_{\mathrm{SA}}$	Gaussian centred at LA-fitted spectral index with $\sigma = $ LA error, or prior based on 10C, see Section 4.2
Source flux density $(S_0/Jy) < 4\sigma_{\mathrm{SA}}$	Delta-function at LA value, unless close to cluster
Source spectral index when $S_0 < 4\sigma_{\mathrm{SA}}$	Delta-function centred at LA-fitted spectral index, or based on 10C, see Section 4.2

source environment and takes full account of the power spectrum of the primordial CMB structure as a function of angular scale as seen by AMI, thermal noise in the *uv*-data, and confusion noise, in the form of a generalised noise covariance matrix. Concatenated SA visibilities must first be binned to reduce the size of the data, easing memory demands; for minimal loss of information, bin sizes are less than aperture illumination function FWHM.

4.1 Modelling

The model we employ for this analysis is described in Olamaie, Hobson, & Grainge (2012) and Olamaie, Hobson, & Grainge (2013), and is based on a number of key assumptions. The first two are the functional forms of the dark matter density profile and the gas pressure profile within a spherical geometry. The non-baryonic matter distribution of a cluster is described using a NFW model,

$$\rho_{\mathrm{DM}}(r) = \frac{\rho_{\mathrm{s}}}{\left(\frac{r}{R_{\mathrm{s}}}\right)\left(1 + \frac{r}{R_{\mathrm{s}}}\right)^2}, \qquad (3)$$

where ρ_{s} is an overall normalisation coefficient and the scale radius, R_{s}, is the value of r at which $\mathrm{d}\ln\rho(r)/\mathrm{d}\ln r = -2$. A GNFW model is used to describe the gas pressure profile

$$P_{\mathrm{e}}(r) = \frac{P_{\mathrm{ei}}}{\left(\frac{r}{r_{\mathrm{p}}}\right)^c \left(1 + \left(\frac{r}{r_{\mathrm{p}}}\right)^a\right)^{(b-c)/a}}, \qquad (4)$$

where P_{ei} is an overall normalisation coefficient, and r_{p} is the scale radius. The parameters a, b and c describe the slopes of the pressure profile at $r \approx r_{\mathrm{p}}$, $r > r_{\mathrm{p}}$ and $r \ll r_{\mathrm{p}}$ respectively.

The third assumption is of hydrostatic equilibrium throughout the cluster. The final assumption is that the gas mass fraction $f_{\mathrm{gas},r_{200}}$ is small compared to unity, so that $M_{\mathrm{tot},r} \approx M_{\mathrm{DM},r}$. These assumptions allow the total mass within a radius r to be derived as

$$
\begin{aligned}
M_{\mathrm{tot},r} &= \int_0^r \rho_{\mathrm{DM}}(r')(4\pi r'^2 \mathrm{d}r') \\
&= 4\pi\rho_{\mathrm{s}}R_{\mathrm{s}}^3 \left\{\ln\left(1 + \frac{r}{R_{\mathrm{s}}}\right) - \left(1 + \frac{R_{\mathrm{s}}}{r}\right)^{-1}\right\}.
\end{aligned} \qquad (5)
$$

Using the assumption of HSE, the electron number density profile $n_{\mathrm{e}}(r)$ can be found and, taking the gas to be ideal, the elec-

tron temperature profile is calculated by $k_{\mathrm{B}}T(r) = P_{\mathrm{e}}(r)/n_{\mathrm{e}}(r)$,

$$
\begin{aligned}
k_{\mathrm{B}}T(r) &= (4\pi\mu G\rho_{\mathrm{s}})(R_{\mathrm{s}}^3) \times \\
&\left[\frac{\ln\left(1 + \frac{r}{R_{\mathrm{s}}}\right) - \left(1 + \frac{R_{\mathrm{s}}}{r}\right)^{-1}}{r}\right] \times \\
&\left[1 + \left(\frac{r}{r_{\mathrm{p}}}\right)^a\right]\left[b\left(\frac{r}{r_{\mathrm{p}}}\right)^a + c\right]^{-1}.
\end{aligned} \qquad (6)
$$

Parameter values are estimated at or within an overdensity radius r_Δ, the cluster radius internal to which the mean density is Δ times the critical density at the cluster redshift. Throughout this paper we use parameters estimated from this model at or within r_{200} and r_{500}.

4.2 Priors

Priors are summarised in Table 4. The prior on cluster total mass is based on statistics of cluster masses and AMI observing capabilities. The prior on the gas fraction at r_{200}, denoted $f_{\mathrm{gas},r_{200}}$, is tight as SZ data do not contrain this property: our priors are based on X-ray studies and WMAP, see e.g. Vikhlinin et al. (2006) Vikhlinin et al. (2009a) and Komatsu et al. (2011). The shape parameters a, b, c, and c_{500} are given delta priors at the "universal" values from Arnaud et al. (2010), who assign these parameters the values $a = 1.0510$, $b = 5.4905$, $c = 0.3081$ and $c_{500} = 1.177$. Imposing a fixed pressure profile shape to all sample members, we expect the derived cluster parameters to be highly correlated; this is discussed further in Section 6.

Priors on the radio point source parameters $(x_{\mathrm{s}}, y_{\mathrm{s}}, S_0, \alpha_{\mathrm{s}})$ are taken from source-finding in the LA maps, as described in Section 3, and are dependent on the detection significance of the source in the SA map. For all point sources, priors on position $(x_{\mathrm{s}}, y_{\mathrm{s}})$ are set as delta functions to the LA values due to the much higher resolution of the LA. Sources detected at $> 4\sigma_{\mathrm{SA}}$ are given Gaussian priors on the LA flux estimate and the spectral index (either fitted from the LA channel data or based on the 10C survey.) These parameters are modeled simultaneously by McAdam with the cluster parameters to account for possible flux calibration errors between the arrays and source variability between observations, discussed earlier. Sources detected at $< 4\sigma_{\mathrm{SA}}$ are given delta-priors on LA flux and spectral index, but where the source position is close to the cluster centre, we replace delta priors with Gaussian priors as detailed in Table 4.

Table 5. Some MCADAM derived large-scale cluster parameter values for the AMI-CLASH sub-sample, internal to r_{200}. $T_{SZ}(r_{200})$ is the gas temperature at r_{200}. Uncertainties are 68 per cent confidence uncertainties (1σ). "/" means "in units of". Due to the strong correlations between the parameters, their uncertainties are also correlated.

Cluster	$M_{\text{tot},r_{200}}$ /$(10^{14}M_\odot)$	$M_{\text{gas},r_{200}}$ /$(10^{14}M_\odot)$	r_{200} / Mpc	$T_{SZ}(r_{200})$ / keV	$Y_{r_{200}}$ /(10^{-4}Mpc^{-2})	Redshift
A611	7.7 ± 1.1	0.99 ± 0.10	1.71 ± 0.08	3.3 ± 0.3	0.67 ± 0.11	0.288
A1423	4.5 ± 1.1	0.57 ± 0.14	1.46 ± 0.12	2.2 ± 0.4	$0.28^{+0.10}_{-0.09}$	0.213
A2261	13.3 ± 1.9	1.69 ± 0.08	2.10 ± 0.10	$4.6^{+0.5}_{-0.4}$	$1.58^{+0.19}_{-0.17}$	0.224
CLJ1226+3332	4.9 ± 1.1	0.62 ± 0.14	1.15 ± 0.09	3.1 ± 0.5	0.36 ± 0.13	0.890
MAJ0647+7015	$11.4^{+1.5}_{-1.4}$	1.41 ± 0.11	1.74 ± 0.07	4.8 ± 0.4	1.27 ± 0.16	0.584
MAJ0717+3745	12.9 ± 1.8	1.65 ± 0.16	1.84 ± 0.09	5.2 ± 0.5	1.60 ± 0.25	0.548
MAJ0744+3927	11.5 ± 1.4	1.50 ± 0.12	1.68 ± 0.07	5.1 ± 0.4	1.40 ± 0.17	0.686
MAJ1149+2223	15.7 ± 1.7	2.00 ± 0.11	1.97 ± 0.07	5.9 ± 0.4	2.20 ± 0.20	0.544
MAJ1423+2404	$7.7^{+2.1}_{-2.3}$	$0.99^{+0.26}_{-0.27}$	1.54 ± 0.15	3.6 ± 0.7	$0.72^{+0.29}_{-0.30}$	0.545
RXJ1532+3021	5.6 ± 1.8	$0.73^{+0.22}_{-0.23}$	$1.49^{+0.16}_{-0.17}$	2.7 ± 0.6	$0.42^{+0.20}_{-0.21}$	0.345
MAJ0717 RH	14.1 ± 1.9	1.80 ± 0.16	1.89 ± 0.09	5.5 ± 0.5	1.85 ± 0.27	0.548

Table 6. Same as Table 5 for cluster parameter estimates at, or internal to, r_{500}.

Cluster	$M_{\text{tot},r_{500}}$ /$(10^{14}M_\odot)$	$M_{\text{gas},r_{500}}$ /$(10^{14}M_\odot)$	r_{500} / Mpc	$T_{SZ}(r_{500})$ / keV	$Y_{r_{500}}$ /(10^{-4}Mpc^{-2})
A611	5.7 ± 0.8	0.69 ± 0.07	1.14 ± 0.06	4.0 ± 0.4	0.51 ± 0.08
A1423	3.3 ± 0.8	0.39 ± 0.09	0.98 ± 0.08	2.8 ± 0.5	0.21 ± 0.08
A2261	9.8 ± 1.4	$1.17^{+0.05}_{-0.06}$	1.40 ± 0.07	5.6 ± 0.5	$1.20^{+0.14}_{-0.13}$
CLJ1226+3332	3.6 ± 0.8	0.45 ± 0.10	0.77 ± 0.06	3.6 ± 0.6	0.27 ± 0.10
MAJ0647+7015	8.4 ± 1.1	1.00 ± 0.08	1.16 ± 0.05	5.6 ± 0.5	0.97 ± 0.12
MAJ0717+3745	9.6 ± 1.3	1.17 ± 0.11	1.23 ± 0.06	$6.1^{+0.5}_{-0.6}$	1.22 ± 0.19
MAJ0744+3927	8.5 ± 1.0	1.07 ± 0.09	1.12 ± 0.05	5.9 ± 0.5	1.10 ± 0.13
MAJ1149+2223	11.6 ± 1.3	1.42 ± 0.08	1.31 ± 0.05	6.9 ± 0.5	1.67 ± 0.15
MAJ1423+2404	5.7 ± 1.6	0.70 ± 0.19	1.03 ± 0.10	4.3 ± 0.8	$0.55^{+0.22}_{-0.23}$
RXJ1532+3021	$4.2^{+1.3}_{-1.4}$	0.51 ± 0.16	1.00 ± 0.11	3.3 ± 0.7	0.32 ± 0.16
MAJ0717 RH	10.4 ± 1.4	$1.30^{+0.12}_{-0.14}$	1.26 ± 0.06	6.4 ± 0.6	1.40 ± 0.21

5   SZ MAPS AND PHYSICAL PARAMETERS

In this section we present maps and probability distributions, and discuss each cluster individually. Tables 5 and 6 summarise some key MCADAM-estimated parameter values. Table 5 also includes cluster spectroscopic redshifts. The naturally-weighted SA maps shown in Figures 1 to 10 are non-source-subtracted (the left of each Figure) and source-subtracted (the right of each Figure). Contour levels correspond to $\pm 3\sigma_{\text{SA}}$ to $\pm 10\sigma_{\text{SA}}$, where solid contours indicate positive emission and dashed contours indicate decrement. The half-power contour of the synthesized beam for each map is displayed in the bottom left-hand corner. No primary beam correction or uv-taper has been applied. In the source-subtracted maps the sources that are given Gaussian priors on flux density and spectral index are indicated by '×' and those modeled with delta priors by '+'. The SZ fitted cluster centre position is marked with a □.

On the parameter probability distributions, in Figures 1 to 10, the green lines and crosses show the mean and the contour levels represent 68 per cent and 95 per cent confidence limits. The 2D marginalised posterior distributions show the degeneracies between parameter values and the correlations between uncertainties. We emphasise that derived parameters and their uncertainties are correlated – this is important in Sections 6 and 7. Where necessary we consider possible degeneracies between the fitted cluster parameters and the fluxes of sources very close to the cluster centre; such degeneracy depends on the source position relative to the cluster centre and on the brightness of the source.

As stated in Section 4.2, SZ data provide little constraint on the value of $f_{\text{gas},r_{200}}$. This is demonstrated in the bottom right panel of Figure 1 where we plot the 1D marginalised $f_{\text{gas},r_{200}}$ posterior overlaid with its prior. For comparison, we also plot the 1D marginalised $M_{\text{tot},r_{200}}$ posterior overlaid with its prior.

5.1   A611

The SZ decrement is clearly visible in both un-subtracted and source-subtracted SA maps . Source subtraction produces a map with very few residuals, and with no sources appearing at the cluster centre we expect the source environment has negligible effect on fitted cluster parameters.

5.2   A1423

The complicated source environment has been subtracted successfully – there are no sources > 2 mJy close to the cluster SZ decrement, which is visible in the source subtracted map at a high significance. Residuals in the source-subtracted map suggest some extended emission in the field that is not visible to the higher resolu-
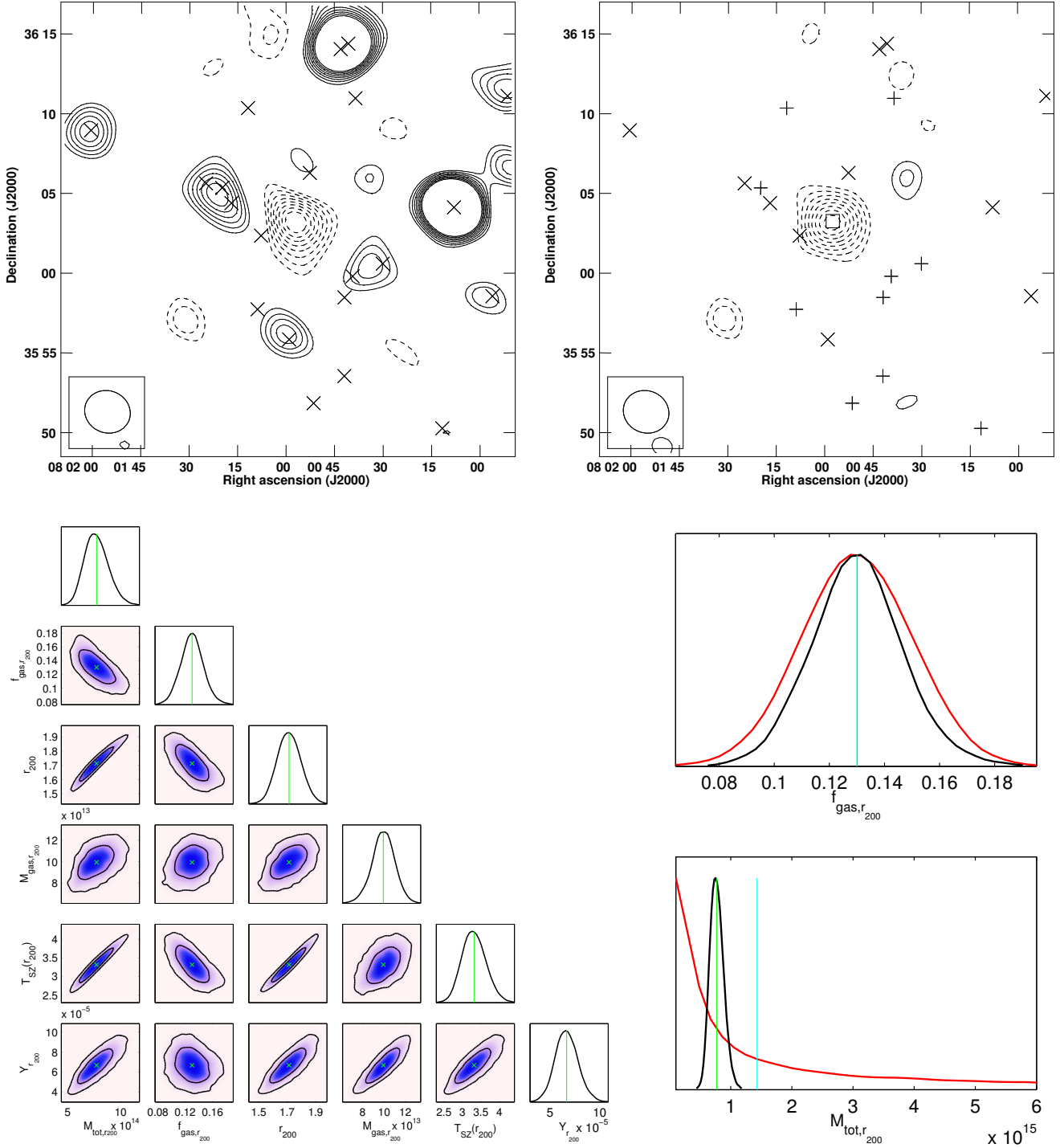
Figure 1. **A611**. Top two panels: SA contour maps – left shows the non-source-subtracted map ($\sigma_{SA} = 89\,\mu$Jy) with crosses showing the positions of LA sources, right shows the source subtracted map ($\sigma_{SA} = 88\,\mu$Jy, $11\sigma_{SA}$ decrement) with crosses marking positions of sources that have been modelled by McAdam and plus signs showing those given delta priors on flux as well as position. Solid contours are positive emission, dashed are negative. Bottom left panel: McAdam fitted parameter probability distributions, the green lines and crosses show the mean and the contour levels represent 68 per cent and 95 per cent confidence limits. Bottom right panel: 1D marginalised posterior distributions for $f_{gas,\,r_{200}}$ (upper) and $M_{tot,\,r_{200}}$ (lower) (as shown in the bottom left panel) overlaid with the priors in red. Fitted mean values are shown in green and prior mean values in cyan.

tion of the LA, but is far enough from the cluster centre to have little or no effect on the estimated parameter values. There is some degeneracy between the flux of the source closest to the cluster centre and the estimated parameter values; although the source flux is low, ≈ 0.5 mJy, and the cluster is resolved, the analysis struggles to sep-

arate the relative contributions of a source and a cluster of small angular size.
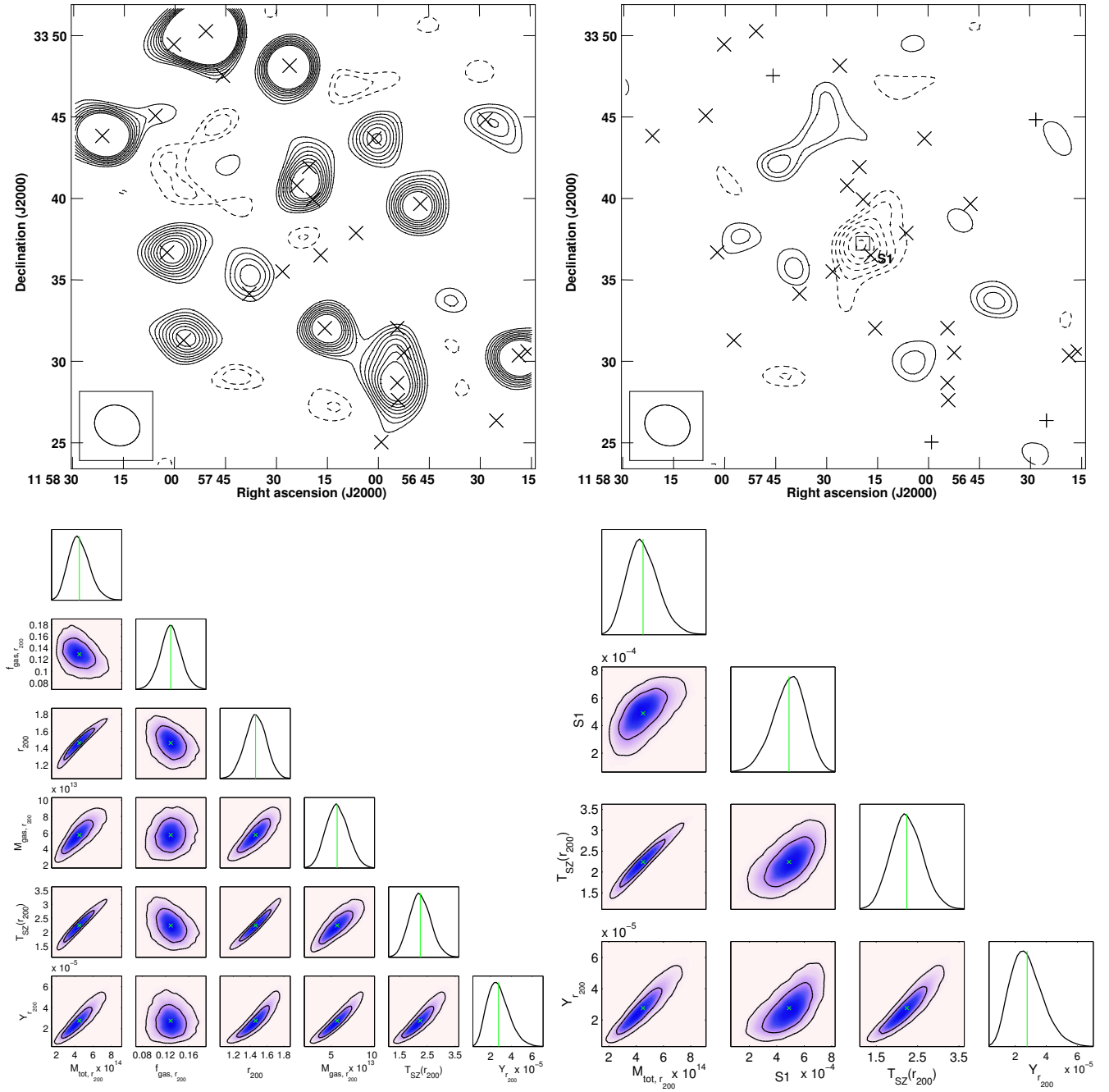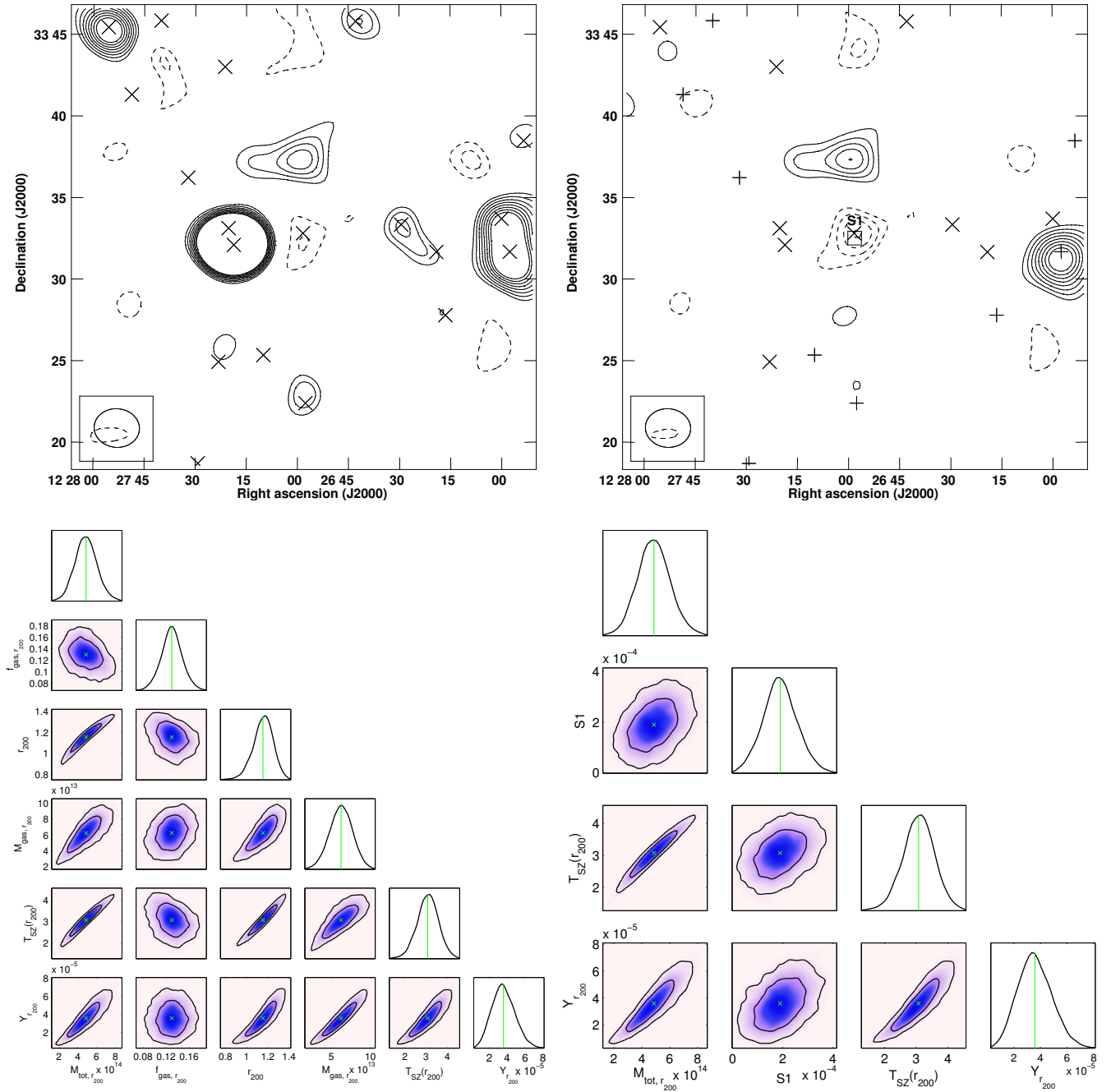
Figure 2. A1423. Top two panels: SA contour maps – left shows the non-source-subtracted map ($\sigma_{SA} = 63\,\mu$Jy), right shows the source subtracted map ($\sigma_{SA} = 62\,\mu$Jy, $8\sigma_{SA}$ decrement). See Figure 1 caption for more details. Bottom two panels: MᴄAᴅᴀᴍ fitted probability distributions – left shows parameter probability distributions, right shows degeneracies between the fitted cluster parameter values and the flux of source S1, labelled on the map in the top right panel. The green lines and crosses show the mean and the contour levels represent 68 per cent and 95 per cent confidence limits.

5.3 A2261

This very massive cluster has a particularly complicated source environment with many sources up to 20 mJy. A particularly deep, more-uniform noise level over the whole LA map was needed to characterise the sources sufficiently accurately in order to describe the source environment to MᴄAᴅᴀᴍ without confusion due to side lobes. In our initial analysis, the source environment was inaccurately described due to exclusion zones automatically placed

by Sᴏᴜʀᴄᴇ-Fɪɴᴅ around bright sources, within which other sources were not modelled. With the exclusion zones removed, the source environment was accurately modelled and the cluster analysed again, with the updated source information. The large number of sources – and consequent high dimensionality – necessitated the use of the next generation sampler PᴏʟʏCʜᴏʀᴅ (Handley, Hobson, & Lasenby 2015a and Handley, Hobson, & Lasenby 2015b) in the place of MᴜʟᴛɪNᴇsᴛ. There is very little difference between the parameter values estimated by the MᴜʟᴛɪNᴇsᴛ and PᴏʟʏCʜᴏʀᴅ ana-
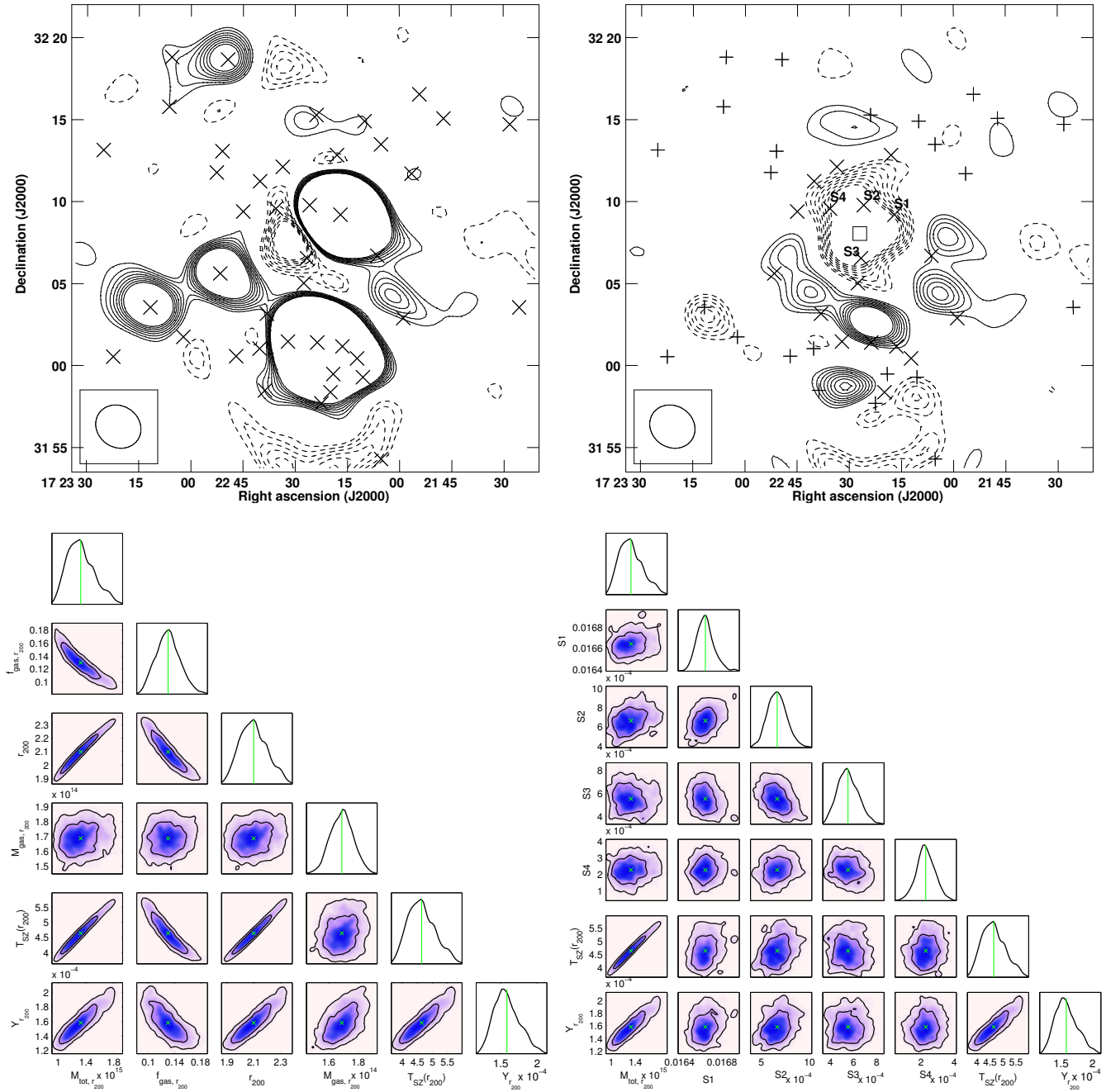
Figure 3. A2261. Top two panels: SA contour maps – left shows the ($\sigma_{SA} = 68\,\mu$Jy), right shows the source subtracted map ($\sigma_{SA} = 67\,\mu$Jy, $22\sigma_{SA}$ decrement). See Figure 1 caption for more details. Bottom two panels: McADAM fitted probability distributions – left shows parameter probability distributions, right shows degeneracies between the fitted cluster parameter values and the flux of sources S1, S2, S3, and S4, labelled on the map in the top right panel. The green lines and crosses show the mean and the contour levels represent 68 per cent and 95 per cent confidence limits.

lyses, showing that our analysis is robust against the presence of bright sources at ≈ 7 arcmin from the cluster centre. Closer to the cluster centre there are other sources; for the four closest we find negligible degeneracies between the source fluxes and the SZ parameter values. This is particularly noteworthy for source S_1 which has a flux of nearly 17 mJy but, as a point source, is easily distinguished in the analysis from the very extended cluster. Although there are significant residuals in the source-subtracted map they are

far enough from the very large SZ decrememt that our parameter estimates are negligibly affected.

5.4 CLJ1226+3332

This is the highest redshift cluster in the CLASH sample at $z = 0.888$ and also one of the least massive. Although the source environment is largely sparse, there is a low-significance source
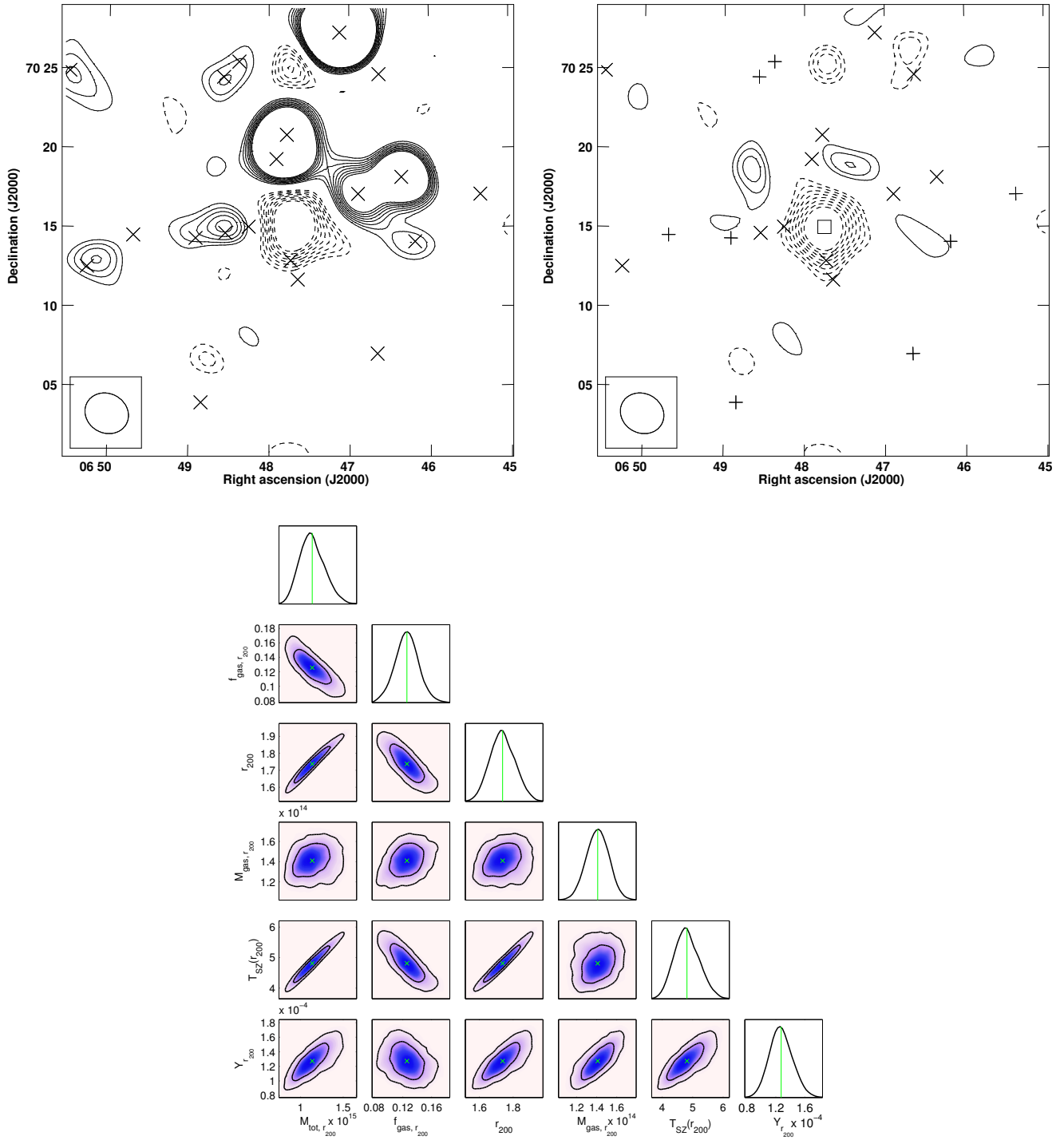
Figure 4. **CLJ1226+3332**. Top two panels: SA contour maps – left shows the non-source-subtracted map ($\sigma_{SA} = 82\,\mu$Jy), right shows the source subtracted map ($\sigma_{SA} = 80\,\mu$Jy, $6\sigma_{SA}$ decrement). See Figure 1 caption for more details. Bottom two panels: McAdam fitted probability distributions – left shows parameter probability distributions, right shows degeneracies between the fitted cluster parameter values and the flux of source S1, labelled on the map in the top right panel. The green lines and crosses show the mean and the contour levels represent 68 per cent and 95 per cent confidence limits.

directly on the cluster X-ray centre. This is a particular concern for CLJ1226+3332 due to its high redshift and, therefore, small angular size: there is a larger degeneracy than is typical in the AMI-CLASH sub-sample, for a source of such low flux density (≈ 0.18 mJy) close to the cluster centre. Useful parameter constraints are still obtained, as is illustrated by Figure 4, bottom right, where the marginalised posteriors take full account of the degeneracies.

5.5 MAJ0647+7015 – strong-lensing selected

The SZ decrement is clearly visible in both unsubtracted and subtracted SA maps. Our unsubtracted AMI maps show a source environment with no sources near the cluster centre and only sources of < 4 mJy towards the edge of the cluster decrement. The single bright source in the field is 21 mJy but is ≈ 12 arcmin from the cluster centre so has negligible effect on parameter estimation.
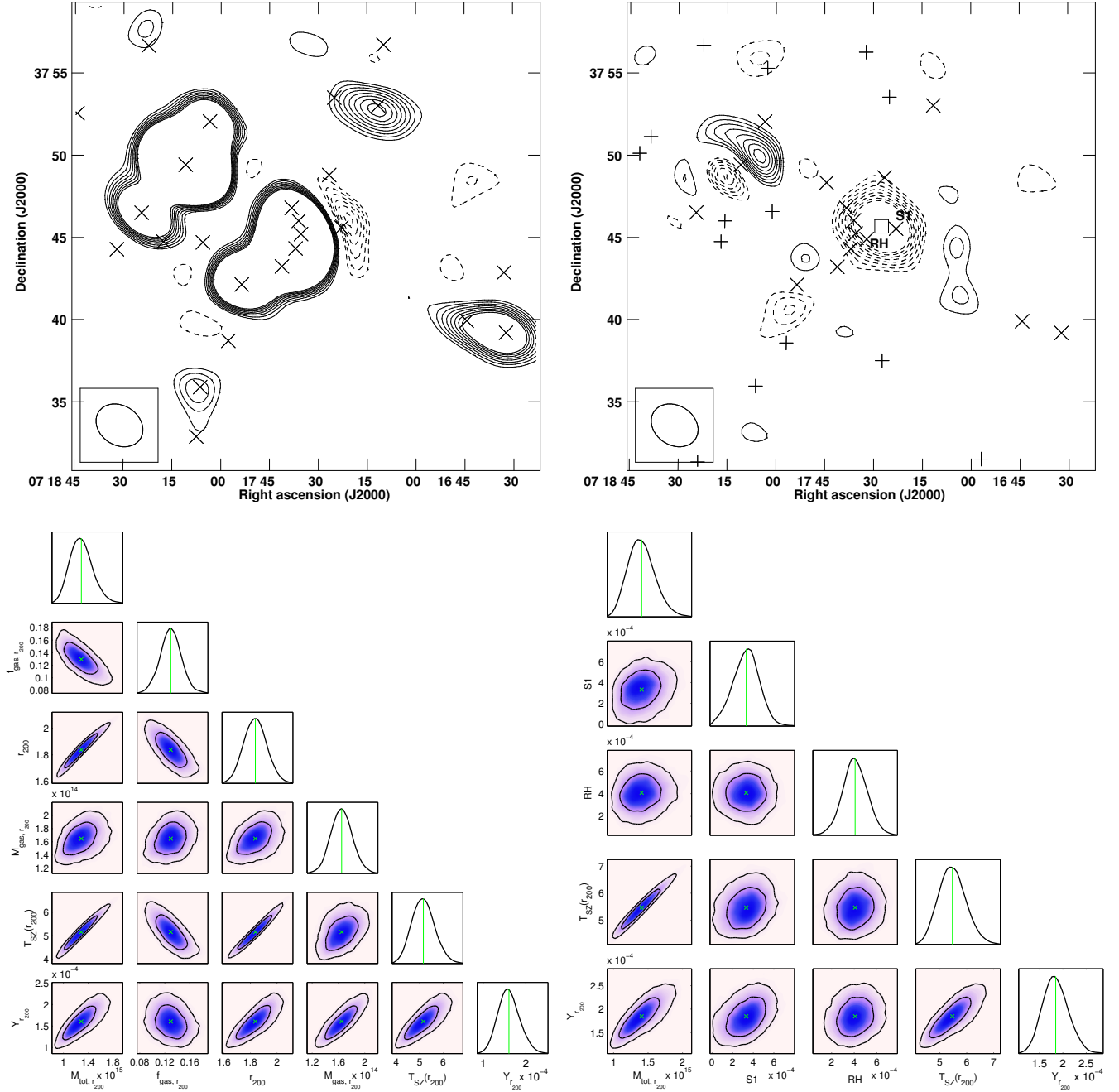
Figure 5. MAJ0647+7015. Top two panels: SA contour maps – left shows the non-source-subtracted map ($\sigma_{SA} = 81\,\mu$Jy), right shows the source subtracted map ($\sigma_{SA} = 80\,\mu$Jy, $14\sigma_{SA}$ decrement). See Figure 1 caption for more details. Bottom panel: McADAM fitted parameter probability distributions, the green lines and crosses show the mean and the contour levels represent 68 per cent and 95 per cent confidence limits.

5.6   MAJ0717+3745 – strong-lensing selected

This source environment requires special consideration. In the LA map we see a set of > 5 mJy point sources near the X-ray centre of the cluster. Amongst these sources there is a slightly extended feature that the map-plane SOURCE-FIND cannot detect. This cluster is known to host a radio halo (see e.g. Zwart et al. 2011, Feretti et al.

2012) and comparing this AMI feature to the 1.4-GHz WSRT map from van Weeren et al. (2009) we consider the possibility that this feature is the radio halo at AMI frequencies. We have investigated how sensitive our parameter estimation is to the flux density of this feature by running the analysis twice with and without a source of 0.34 mJy (measured from the LA map) at the peak position of the feature (labeled RH on the subtracted SA map). The additional flux
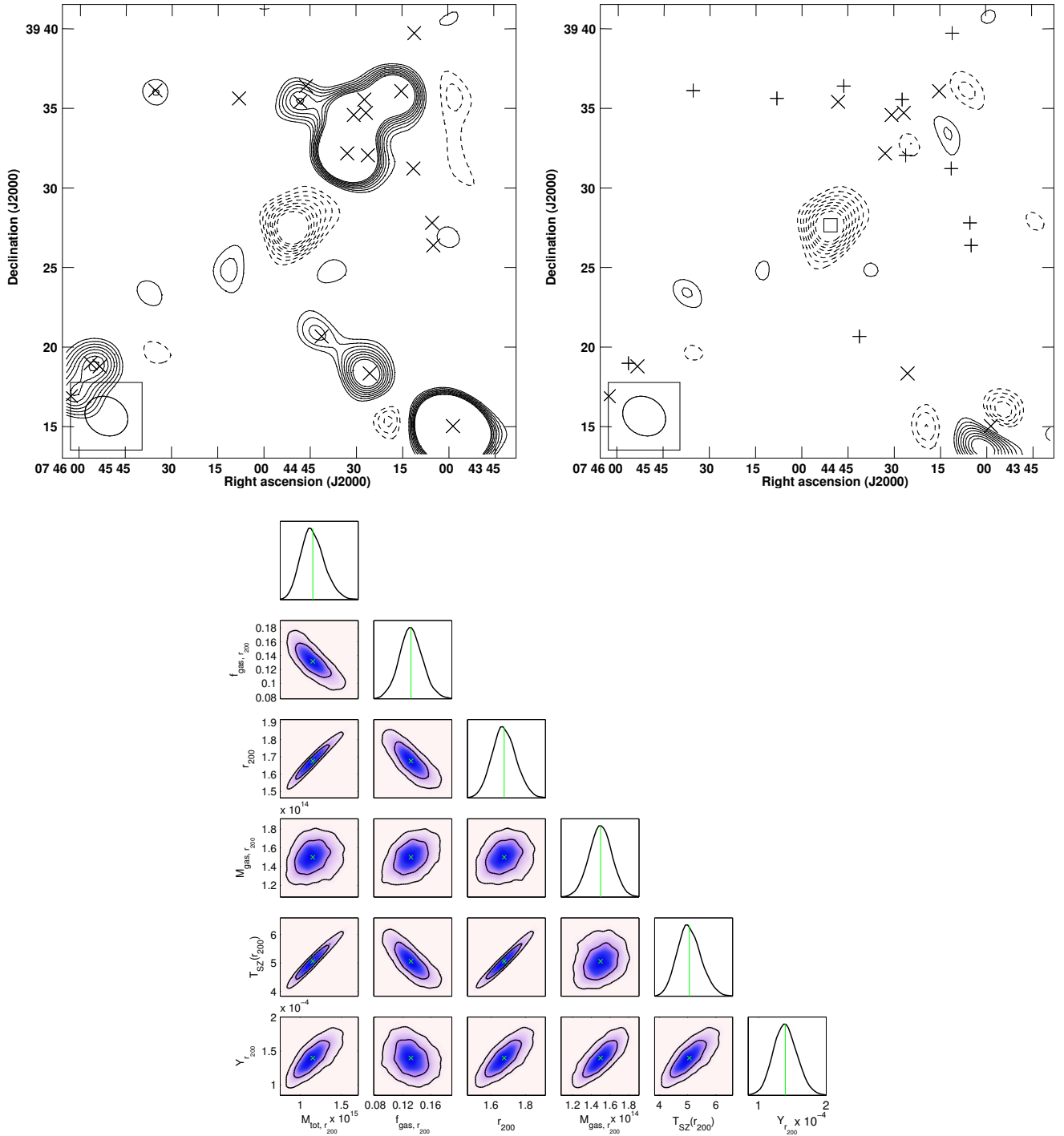
Figure 6. **MAJ0717+3745**. Top two panels: SA contour maps – left shows the non-source-subtracted map ($\sigma_{SA} = 84\,\mu Jy$), right shows the source subtracted map ($\sigma_{SA} = 82\,\mu Jy$, $18\sigma_{SA}$ decrement). See Figure 1 caption for more details. Bottom two panels: McADAM fitted probability distributions – left shows parameter probability distributions, right shows degeneracies between the fitted cluster parameter values and the flux of source S1 and possible radio halo remnant RH, labelled on the map in the top right panel. The green lines and crosses show the mean and the contour levels represent 68 per cent and 95 per cent confidence limits.

raises estimates of Y-values, masses and temperatures by less than 1σ and the map decrement by less than 2σ. There is no degeneracy between parameter values and the additional flux and none associated with the sources closest to the cluster centre. The additional analysis is referred to as MAJ0717RH in the rest of this paper.

5.7 MAJ0744+3927

We estimate MAJ0744+3927 to be among the more massive members of the sub-sample, and it has the second highest redshift in the complete CLASH sample. The source environment is not troublesome, with no sources detected near the cluster centre. The sources lying away from the cluster decrement are subtracted to leave very few residuals.
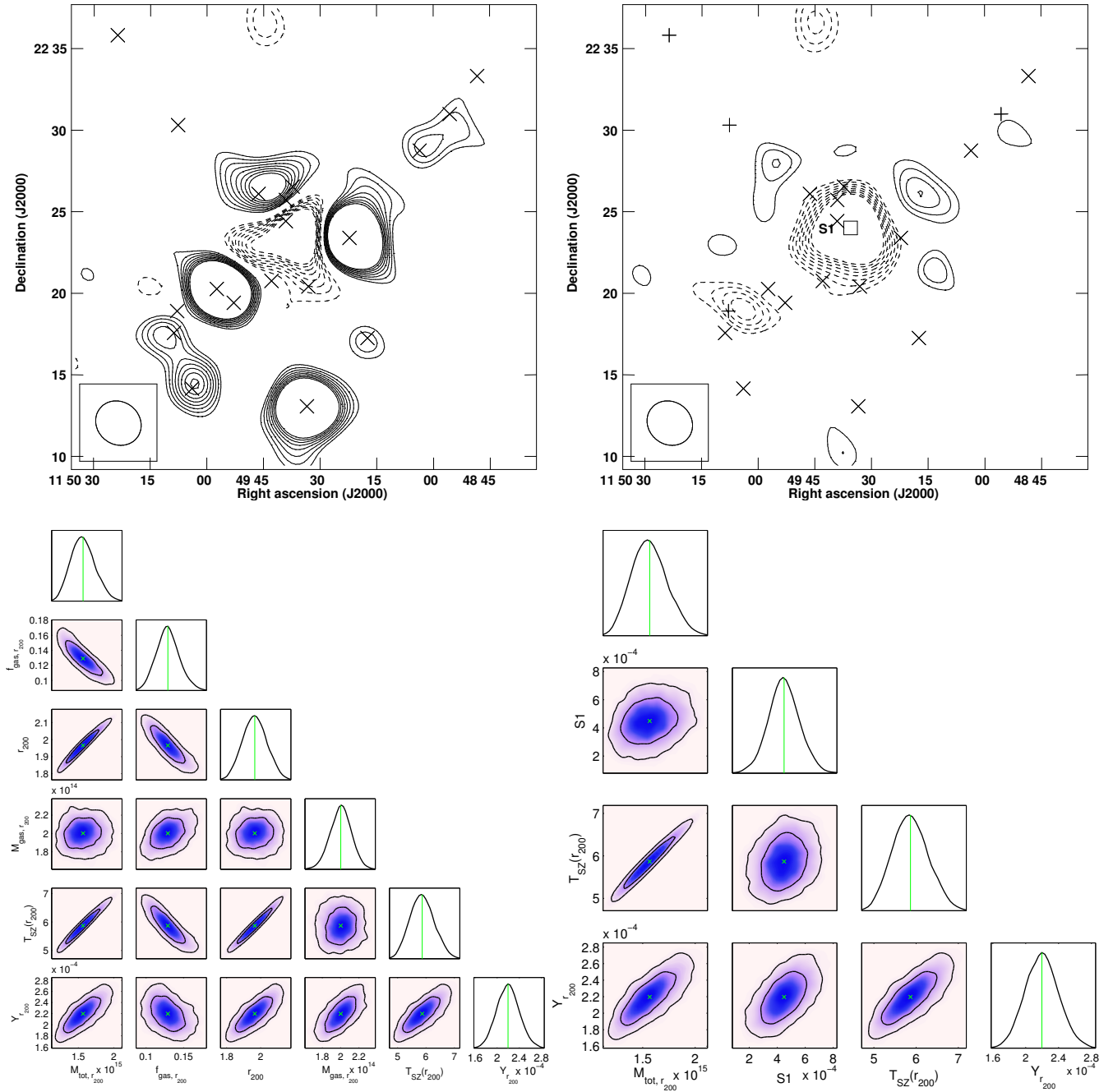
Figure 7. MAJ0744+3927. Top two panels: SA contour maps – left shows the non-source-subtracted map ($\sigma_{SA} = 92\,\mu$Jy), right shows the source subtracted map ($\sigma_{SA} = 91\,\mu$Jy, $13\sigma_{SA}$ decrement). See Figure 1 caption for more details. Bottom panel: McADAM fitted parameter probability distributions, the green lines and crosses show the mean and the contour levels represent 68 per cent and 95 per cent confidence limits.

5.8   MAJ1149+2223 – strong-lensing selected

Parameter estimation reveals this to be the most massive cluster in our AMI-CLASH sub-sample, with a large angular extent, despite its redshift. The radio source environment is fitted and subtracted well, leaving only a few residuals in the map which do not significantly affect the parameter estimation. We have checked the source closest to the cluster centre for degeneracy with the estim-

ated cluster parameter values and find very little, as expected given the low flux density of the source and the large angular size of the cluster.

Figure 8. **MAJ1149+2223**. Top two panels: SA contour maps – left shows the non-source-subtracted map (σ_{SA} = 77 μJy), right shows the source subtracted map (σ_{SA} = 75 μJy, 27σ_{SA} decrement). See Figure 1 caption for more details. Bottom two panels: McAdam fitted probability distributions – left shows parameter probability distributions, right shows degeneracies between the fitted cluster parameter values and the flux of source S1, labelled on the map in the top right panel. The green lines and crosses show the mean and the contour levels represent 68 per cent and 95 per cent confidence limits.

5.9 MAJ1423+2404

There are three detected sources lying in the direction of the cluster decrement. The flux densities estimated by McAdam are 2.9 mJy, 0.8 mJy, and 0.15 mJy respectively. The only source close to the cluster centre that shows some degeneracy between the cluster parameter values and its flux density is S_1. The degeneracy is, as usual, taken into account in arriving at the marginalised posteriors.

5.10 RXJ1532+3021

There is a radio source at, and several close to, the map centre, all of which are modelled in McAdam. The source subtraction appears to have been successful with significant residuals only towards the edges of the SA map. We plot the degeneracy of the cluster parameter values with the flux estimates of the two sources closest to the cluster centre. Both sources show some degeneracy, the closer showing a significant amount. As with the other resolved clusters
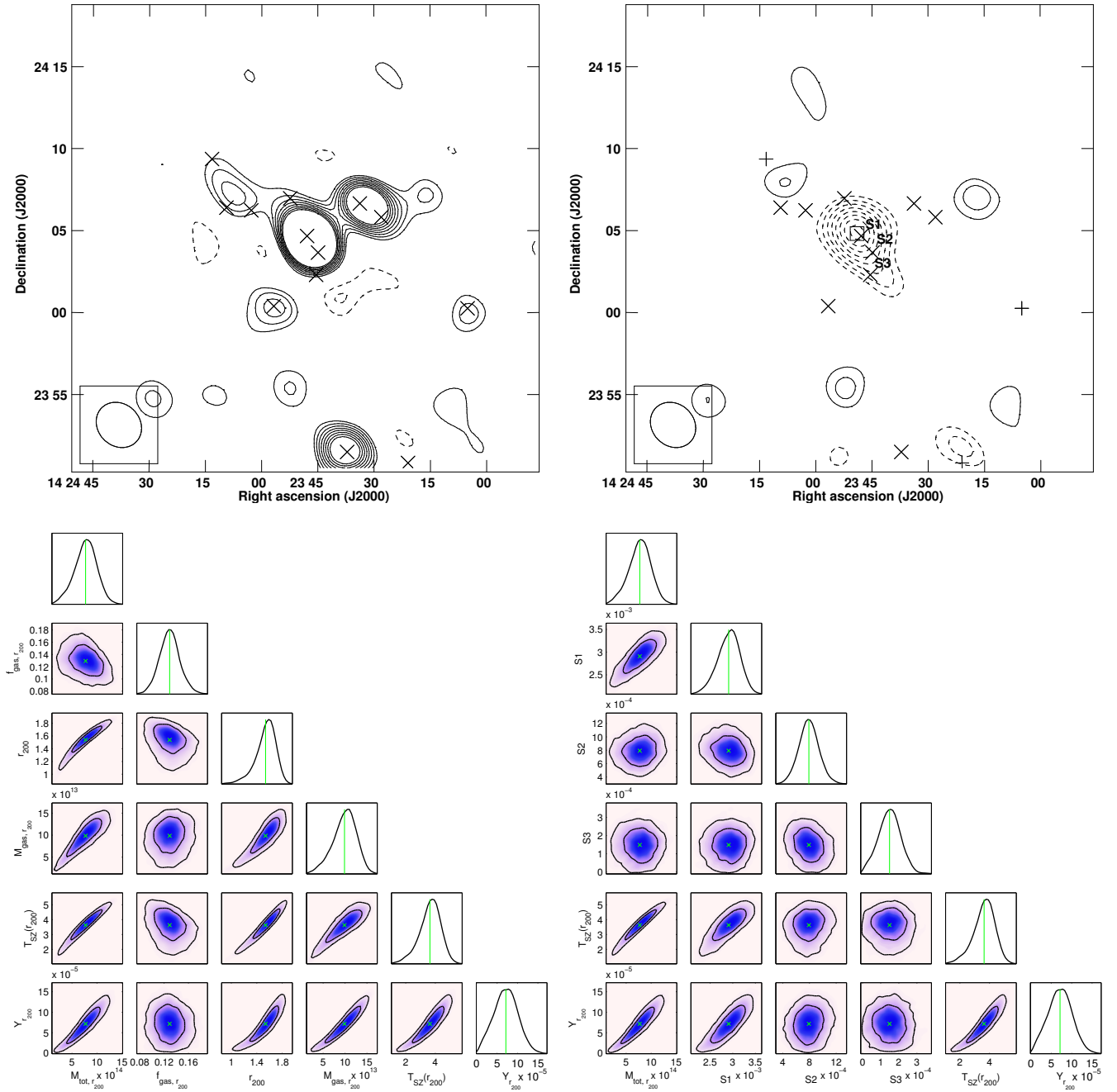
Figure 9. MAJ1423+2404. Top two panels: SA contour maps – left shows the non-source-subtracted map ($\sigma_{SA} = 80\,\mu$Jy), right shows the source subtracted map ($\sigma_{SA} = 80\,\mu$Jy, $10\sigma_{SA}$ decrement). See Figure 1 caption for more details. Bottom two panels: McAdam fitted probability distributions – left shows parameter probability distributions, right shows degeneracies between the fitted cluster parameter values and the flux of sources S1, S2 and S3, labelled on the map in the top right panel. The green lines and crosses show the mean and the contour levels represent 68 per cent and 95 per cent confidence limits.

showing degeneracy with central source fluxes, parameter estimates are still useful as the degeneracy is modelled in the analysis.

6   SELF-SIMILAR SCALING RELATIONS

Assuming self-similarity, the theoretical scaling relations between cluster parameter values should describe the observational relationships, with the scatter dependent only on measurement uncertainties. The predicted *M*–*T* relation is

$$M \propto T^{3/2}, \tag{7}$$

which arises from the potential GM/R being $\propto T$ if all kinetic energy is in gas internal energy, and from $R \propto M^{1/3}$, where M is the total mass within radius R. Similarly, the expected Y–M relation is
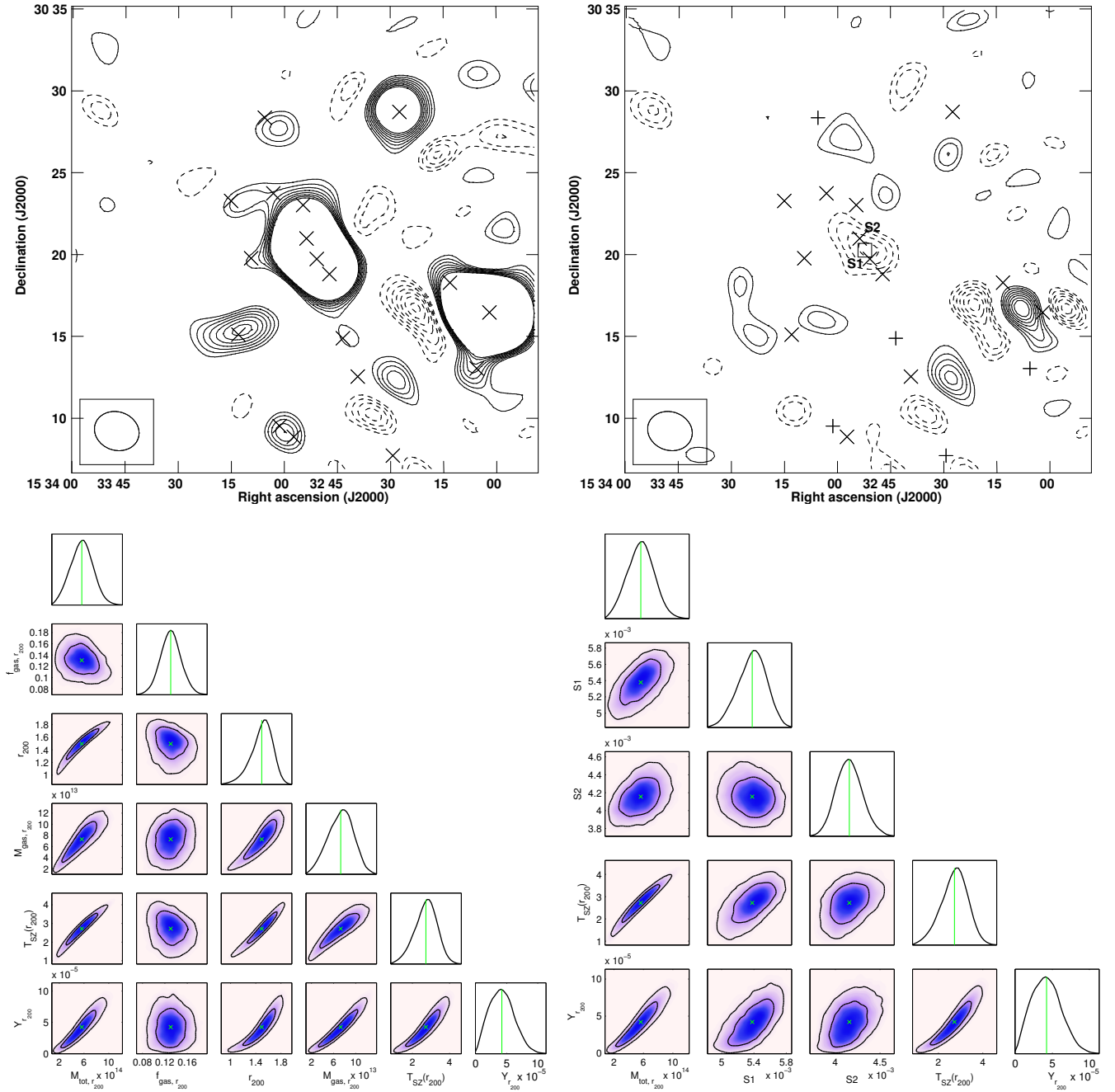
$$Y \propto M^{5/3}. \tag{8}$$

Figure 10. **RXJ1532+3021**. Top two panels: SA contour maps – left shows the non-source-subtracted map ($\sigma_{SA} = 69\,\mu$Jy), right shows the source subtracted map ($\sigma_{SA} = 66\,\mu$Jy, $6\sigma_{SA}$ decrement). See Figure 1 caption for more details. Bottom two panels: McADAM fitted probability distributions – left shows parameter probability distributions, right shows degeneracies between the fitted cluster parameter values and the flux of sources S1 and S2, labelled on the map in the top right panel. The green lines and crosses show the mean and the contour levels represent 68 per cent and 95 per cent confidence limits.

Studies of these scaling relations have been carried out using simulated and real X-ray and SZ data (see e.g. Kravtsov, Vikhlinin, & Nagai 2006, Vikhlinin et al. 2009a, Vikhlinin et al. 2009b, Andersson et al. 2011). Poole et al. (2007) carry out simulations of two-body cluster mergers over a range of mass ratios and impact parameters (see Section 7.2) to investigate the effect of mergers on the scatter in scaling relations by tracking the merger evolution in scaling-relation planes. They find large changes in cluster observables predominantly *along* the scaling-relation, with usually signi-

ficantly less increase in displacement perpendicular to the direction of the relation.

Scaling relations are implicitly present in the model due, e.g., to the assumptions of HSE and pressure profile shape. The relationships between the sampling parameters (see Table 4) and any other derived parameters (e.g. Y, T) are fixed by the model and can be described by power-laws in a similar way to typical scaling relations. We cannot therefore use the relationships between these sampling and derived parameters to investigate the dynamical state
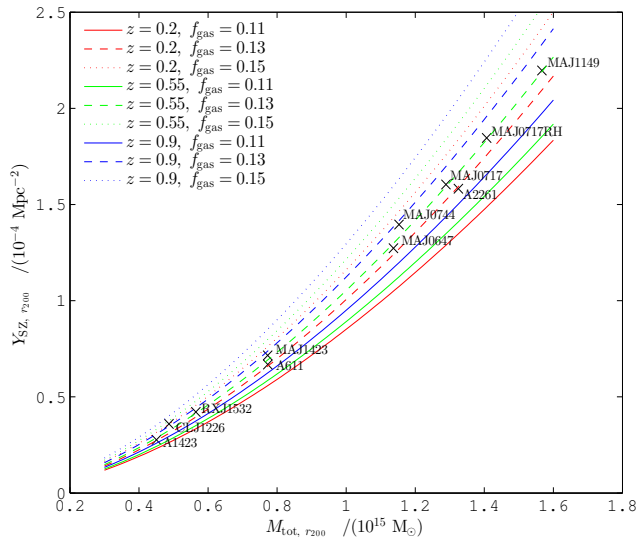
Figure 11. Coloured lines showing $Y_{SZ,r_{200}}$ calculated for a range of $M_{tot,r_{200}}$ values and redshifts consistent with our sample ($3 \leq M_{tot,r_{200}} < 16 \times 10^{14}$ M$_\odot$ and $z = 0.2, 0.55$ and 0.9). $f_{gas,r_{200}}$ varied to its $\pm 1\sigma$ prior values, i.e. 0.11, 0.13 and 0.15 – over-plotted onto the McAdam estimated Y_{SZ} parameter within r_{200} plotted against the estimated total mass within r_{200} for each cluster.
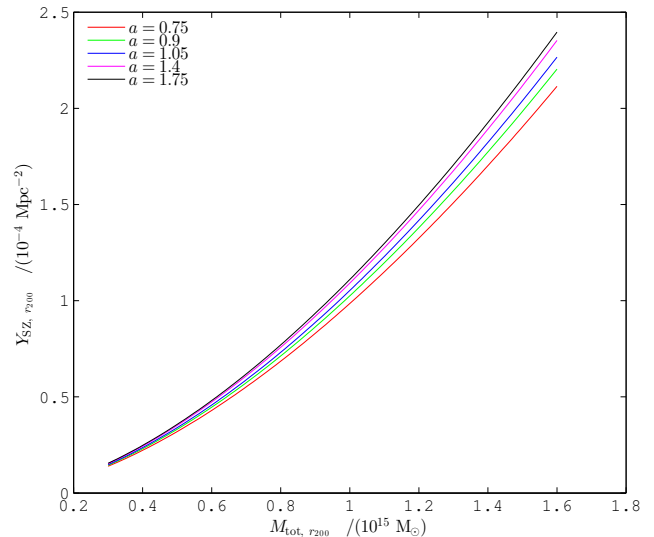
Figure 12. $Y-M$ relations plotted using $M_{tot,r_{200}}$ and $Y_{SZ,r_{200}}$ values calculated with a fixed redshift and $f_{gas,r_{200}}$ of 0.55 and 0.13, respectively. Different coloured lines show different values of a (the shape parameter describing the pressure profile shape around r_{500}) used in the calculation, as listed in the legend.

of a cluster. In Section 6.1 we investigate the correlations in our parameter estimation, focusing on the scaling relation $Y-M$ which is used in further discussions in Section 7.

6.1 $Y-M$

Deviations from these correlations occur because of differences in parameters in the analysis that are independent of the cluster shape parameters, such as the redshift and $f_{gas,200}$. Here, we use the model to demonstrate how these correlations would change if the analysis were sensitive to variations in $f_{gas,200}$, z and shape parameter a, properties that are all given restrictive priors in the analysis (see Section 4.2).

Figure 11 shows theoretical predictions from our model (see Section 4) for the $Y-M$ scaling relation, investigating the implicit relation; we use the model to calculate $Y_{SZ,r_{200}}$ given a range of $M_{tot,r_{200}}$ values and redshifts consistent with our sample, specifically 3×10^{14} M$_\odot \leq M_{tot,r_{200}} < 16 \times 10^{14}$ M$_\odot$ and $z = 0.2, 0.55$ and 0.9. $f_{gas,r_{200}}$ is also varied to its $\pm 1\sigma$ prior values, giving 0.11, 0.13 and 0.15. We have found power-law best-fits $Y = AM^\kappa$, estimating κ and A with an orthogonal linear regression analysis (Isobe et al. 1990), using the Case 3 implementation in the IDL script SIXLIN [2]. As expected, all fits are in good agreement with the self-similar prediction but there are dependencies of A and κ on z and $f_{gas,r_{200}}$ (which is, of course, dependent on mass and redshift). Over-plotted in Figure 11 are the AMI, McAdam-derived, values of $Y_{SZ,r_{200}}$ versus $M_{tot,r_{200}}$. Fitted κ values for $Y = AM^\kappa$ are not dependent on the value of $f_{gas,r_{200}}$ and fitted A values vary by ≈ 25 per cent over the range of $f_{gas,r_{200}}$ values. SZ data provide no constraint on $f_{gas,r_{200}}$ so we use priors from X-ray and WMAP estimates of

this property. Over the prior range the induced deviations of the fitted curves from self-similarity is small. κ and A values are redshift-dependent as $\rho_{crit}(z)$ (the critical density of the Universe at redshift z) and c_{200} (the halo concentration parameter, which is a function of z (Neto et al. 2007)), are used to derive cluster parameters from $M_{tot,r_{200}}$. We find κ and A values change by <0.5 per cent and 10 per cent respectively over the z range used.

Arnaud et al. (2010) (using *XMM-Newton* data) and Planck Collaboration et al. V (2013) (using Planck SZ data), who find average pressure-profile shape parameters, both attribute deviations from the mean values to cluster dynamical state. Poole et al. (2007) show large changes in cluster parameters, such as temperature, mass and luminosity, on Gyr timescales over the course of a merger. It is reasonable to expect the pressure profile, and the inferred shape parameters, to also vary substantially during a merger. This is in agreement with Planck Collaboration et al. II (2013) who fit a wide range of shape parameter values to five disturbed clusters (determined to be disturbed from X-ray morphology).

The assumed geometry and the chosen statistical methodology, in addition to cluster model (including pressure profile shape parameters) and assumptions of e.g. HSE, will also affect dynamical-state dependent parameter estimation. However, our analysis pipeline allows us to investigate the change with dynamical states due to a changes in a. The shape parameter a describes the slope of the pressure profile at radii best constrained by AMI SZ data. We calculate $Y_{SZ,r_{200}}$ given the same range of $M_{tot,r_{200}}$ values. Redshift and $f_{gas,r_{200}}$ are fixed at 0.55 and 0.13 respectively, and a is varied over a range representative of the deviations in a found by Arnaud et al. and Planck Collaboration et al. II: between 0.75 and 1.75. As previously, we have found power-law best-fits for these $Y = AM^\kappa$ curves, plotted in Figure 12. The $Y-M$ fits show very little change in κ as a is changed: less than a per cent over the range of a values. The normalisation, A, changes by less than 15 per cent for $Y = AM^\kappa$. This variation in scaling relations with changing a is indicative of the influence of mergers on scaling relation scatter:

---

[2] Adapted from the FORTRAN script by Isobe et al. (1990). http://idlastro.gsfc.nasa.gov/ftp/pro/math/sixlin.pro

in agreement with Poole et al., the perpendicular scatter caused is small. As AMI data are sensitive to shape parameter a, we could relax the delta prior on a and fit for it in the analysis. However, Figure 12 shows that this would not have much effect on the analysis.

6.2 $Y_{SZ}-Y_{X,AMI}$

A tight relation between Y_X ($\equiv M_{gas}T$) from X-ray and Y_{SZ} (measured directly with an SZ telescope) is predicted from simulation (Kravtsov, Vikhlinin, & Nagai 2006). We next check the tightness of Y_{SZ} (from AMI) versus $Y_{X,AMI}$ (from AMI estimates of M_{gas} and $T_{SZ,mean}$), to facilitate the comparison of $Y_{X,AMI}$ with $Y_{X,Chandra}$ from X-ray studies of our clusters in Section 7. A very tight correlation is expected since both parameters are estimated from the same data, with the same model, and both measure the internal energy of the cluster gas.

The $Y_{SZ}-Y_X$ relation has previously been investigated for real and simulated data, such as Arnaud et al. (2010), Andersson et al. (2011), Rozo, Vikhlinin, & More (2012), and Rozo et al. (2014a), who find $Y_{SZ} \propto Y_X^{\kappa}$ where κ is generally slightly lower than unity.

We derive $Y_{X,AMI}$ from AMI SZ measurements by multiplying our AMI $M_{gas,r_{200}}$ values by our $T_{SZ,mean}$ values, the mean SZ temperature found by taking the average of temperatures calculated with equation 6 in the range $(0.15 < r < 1)r_{200}$. We estimate κ for the AMI-CLASH sub-sample using the orthogonal linear regression analysis (Case 3) used previously. As the uncertainties are highly correlated, we use an analysis that does not take error bars into account. We find $\kappa = 0.978 \pm 0.009$ (where the error is evaluated from the scatter perpendicular to the fitted line) which shows the validity of assuming equivalence of Y_{SZ} and Y_X for our SZ parameter estimation and enables the use of $Y_{X,AMI}$ in comparison with $Y_{X,Chandra}$ values.

7 CLUSTER MERGERS AND SCALING RELATIONS

Both X-ray and SZ studies find scaling relations that largely agree with self-similarity. Scatter about these relations is small, and often attributed to the dynamical states of clusters in the sample used (see e.g. Vikhlinin et al. 2009a, Andersson et al. 2011). Due to the difference in dependence of SZ and X-ray measurement to n_e we expect scatter along scaling relations caused by mergers, predicted by Poole et al. (2007), to be larger for X-ray parameter values than SZ. We next compare AMI SZ parameter values with values from X-ray studies to investigate whether we can demonstrate this observationally.

In Figure 13 we plot two $Y-M$ scaling relations. On the left of Figure 13 we plot AMI parameter values, finding $Y_{X,AMI}$ from $M_{gas,r_{500}}$ and the mean temperature in the range $(0.15 < r < 1)r_{500}$ given by equation 6. On the right of Figure 13 we plot $Y_{X,Chandra}-M_{gas}$ for eight of the AMI-CLASH sub-sample of ten using *Chandra* X-ray estimated parameters from Maughan et al. (2008) (A611 and A1423 are not included in their sample), who calculate M_{gas} internal to r_{500} and find $Y_{X,Chandra}$ from $Y_X = M_{gas}T_X$, where T_X is the mean X-ray temperature in the range $(0.15 < r < 1)r_{500}$. AMI error bars are 68 per cent confidence limits; X-ray error bars are taken from Maughan et al..

SZ and X-ray measurements of a cluster are differently weighted with n_e and T_e. The SZ flux density depends linearly on n_e and T_e whereas the X-ray flux density depends on n_e^2 and $T_e^{1/2}$, where $T_e^{1/2}$ is approximately proportional to the cooling function, $\Lambda(T)$, for the temperatures of the clusters considered here. These

different dependencies will cause parameter values estimated from X-ray to be more influenced by the higher density gas, relative to the SZ estimates. When comparing SZ and X-ray temperatures we reduce this effect by introducing a weighting of $n_e^2 T^{1/2}$ to SZ-derived temperatures. This assumes $n_e(r)$ accurately describes the cluster gas density with no additional density features such as shocking of cluster gas or fractionation. The $Y_{X,AMI}$ values in Figure 13(a) have been calculated with $T_{SZ,mean}$ values weighted in this way.

The behaviour in Figure 13 (a) is, as expected, similar to the $Y-M$ scaling relation in Section 6; in Figure 13 (b) the behaviour is consistent with the self-similar scaling relation but with a substantial scatter. Although our AMI SZ data depends on dynamical state our model (see Section 4.1) does not, as discussed in Section 6.1. The X-ray analysis of Maughan et al. (2008) is dependent on cluster dynamical state, resulting in the scatter seen in Figure 13 (b), showing the sensitivity of X-ray measurement to mergers. AMI values internal to r_{500} produce an orthogonal-linear (Case 3) best-fit to $Y_X \propto M_{gas}^{\kappa}$ with $\kappa = 1.594 \pm 0.025$, from which we have excluded A611 and A1423 in order to match the sample of Maughan et al.. Using X-ray parameter values from Maughan et al., the best-fit value of κ is 1.425 ± 0.091. Over-plotted onto Figure 13 (a) and (b) is the curve of $Y_{X,AMI,r_{500}}$ versus $M_{gas,r_{500}}$ values calculated from our model, as in Section 6.1, with $f_{gas,r_{200}} = 0.13$, $a = 1.05$ and $z = 0.55$.

Both the discussions in the literature, cited in Table 1, and studies showing the strong correlation between lensing strength and merger activity (see e.g. Zitrin et al. 2013), indicate that the three clusters selected for their lensing strength are significantly more disturbed than the remaining seven. In Figure 13(b) these show slightly more deviation from the calculated curve relative to more relaxed systems, consistent with the small increase in perpendicular scatter caused by mergers found by Poole et al. (2007). CLJ1226+3332 also has a small deviation from the curve.

Despite the increase in perpendicular displacements caused by cluster dynamics, shown by Poole et al., X-ray scaling relations, like SZ relations, are seen to be consistent with self-similarity, (see e.g. Vikhlinin et al. 2009a); and indeed, this is what we see when plotting the X-ray parameters from Maughan et al., as illustrated by the over-plotted power-law on the Y_X-M_{gas} plots in Figure 13.

However, the agreement of X-ray and SZ relations is not seen in individual cluster parameters on the Y_X-M_{gas} plots: some cluster positions agree very well in Y_X-M_{gas} space, with very little difference between SZ and X-ray estimated parameter values. Others disagree by 2× or more. Figure 14 shows the ratio of AMI and *Chandra* Y_X values plotted against the ratio of AMI and *Chandra* M_{gas} values and helps show the differences between the plots in Figure 13. In Figure 14, deviations from 1 (marked by dashed lines in each dimension) show differences in the SZ-and X-ray-derived parameter values: the most significant deviations from 1:1 correspond to high values of *Chandra* Y_X and *Chandra* M_{gas}.

Although the β-model, which is used by Maughan et al. (2008), has been shown to produce different estimates of parameter values to the GNFW model when used to analyse AMI SZ data (see Schammel et al. 2013), we do not expect this to produce the discrepancies seen in Figure 14. Recent studies have moved away from using the β-model, favouring the use of NFW and GNFW profiles which give a more detailed description of the changing gradient of the pressure profile over a wide range of r. For the cluster masses and redshifts considered here, X-ray sensitivity is good out to r_{500}. As a β-model gives a good general description of the pressure pro-
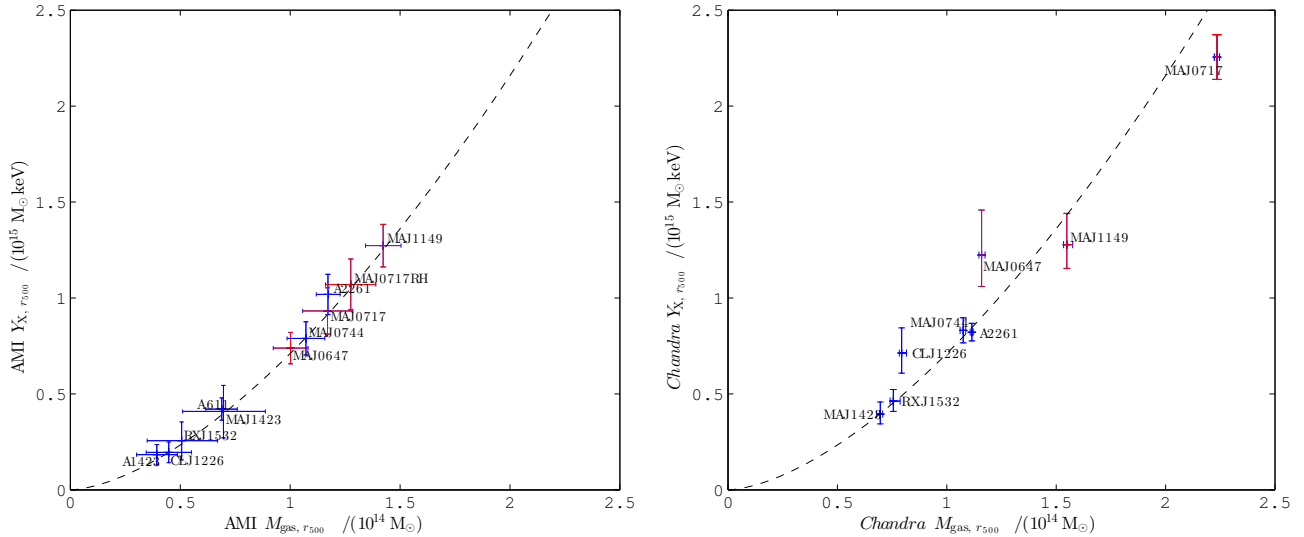
Figure 13. Left (a): Y_X values calculated within r_{500} from AMI estimated parameter values, with T_{SZ} weighted by $n_e^2 T^{1/2}$ (to imitate an X-ray-like weighting to n_e^2 and $T^{1/2}$), plotted against the estimated gas mass within r_{500} for each cluster. Error bars show 68 per cent confidence levels. Right (b): The X-ray estimated Y_X values within r_{500} plotted against the estimated gas mass within r_{500}. Parameter values and errors from Maughan et al. (2008). Strong-lensing-selected sample members are displayed in red. Dashed lines show the Y–M relation of $Y_{X, r_{500}}$ and $M_{gas, r_{500}}$ values calculated from our model with $z = 0.55$, $f_{gas, r_{200}} = 0.13$ and $a = 1.05$.
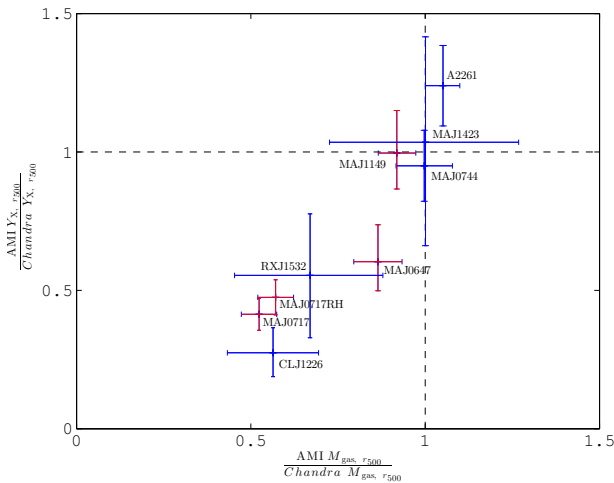
Figure 14. The ratio of AMI and *Chandra* Y_X within r_{500} plotted against the ratio of AMI and *Chandra* M_{gas} within r_{500}, to show discrepancies from deviations of the ratios from 1. $\frac{AMI\ Y_X}{Chandra\ Y_X} = 1$ and $\frac{AMI\ M_{gas}}{Chandra\ M_{gas}} = 1$ are plotted in dashed lines, the intersection of which indicates agreement of parameters. *Chandra* parameter estimates are from Maughan et al. (2008). Errors are calculated from those in Figure 13. Strong-lensing-selected sample members are displayed in red.

file in a relaxed cluster in the range $(0.15 < r < 1)r_{500}$[3], estimates of M_{gas} within this range via a β-model, from good X-ray data, are likely to be robust. A more detailed description of the pressure profile, provided by an NFW-like profile, is required to accurately infer M_{gas} in the range $(0.15 < r < 1)r_{500}$ from AMI SZ data that (for these clusters) have greatest sensitivity to scales r_{500} to r_{200}. It is, therefore, reasonable to expect our AMI SZ parameter estimates to

---

[3] Thus ignoring differences in descriptions of the cluster centre.

agree with those of Maughan et al. for relaxed, high signal-to-noise clusters.

The discrepancies in Y_X, highlighted by Figure 14, show an effect that has not been removed by accounting for the difference in dependence of the SZ and X-ray signals to the density profile $n_e(r)$ also present in M_{gas} estimates. This could result from additional density components such as shocking and/or fractionation in the cluster gas that are not described by $n_e(r)$, and therefore not accounted for when adjusting the SZ temperature. The apparent splitting of sample members into two populations in Figure 14 indicates a systematic effect, whereas simple departures of clusters from relaxed morphology and HSE, assumed in the model, would cause random distributions of clusters about the 1:1 point.

Poole et al. (2007) allow for, e.g., shocking, fractionation and radiative cooling, and show cluster observables evolving during a merger, following paths along the plotted scaling relations with small deviations perpendicular to the relations. The difference in sensitivity of X-ray and SZ measurement to this merger activity allows us to investigate the large displacements along the scaling relation more clearly than looking at deviations of SZ or X-ray cluster parameters from a self-similar relation.

Displaying discrepancies between SZ and X-ray measurements as we do in Figure 14 illustrates the discrepancies between SZ and X-ray temperature estimates in the context of the typical use of cluster parameter estimates. We next compare temperature estimates measured from SZ and X-ray directly.

7.1 T_{SZ} versus T_X

Rodríguez-Gonzálvez et al. (2012) discuss using discrepancies in estimates of cluster temperature between SZ and X-ray to highlight mergers, probing boosts in cluster temperature through shocking and/or fractionation directly. We follow Rodríguez-Gonzálvez et al. and plot the SZ temperature estimated by McAdam against the X-ray temperature from *Chandra* data. Temperature estimates
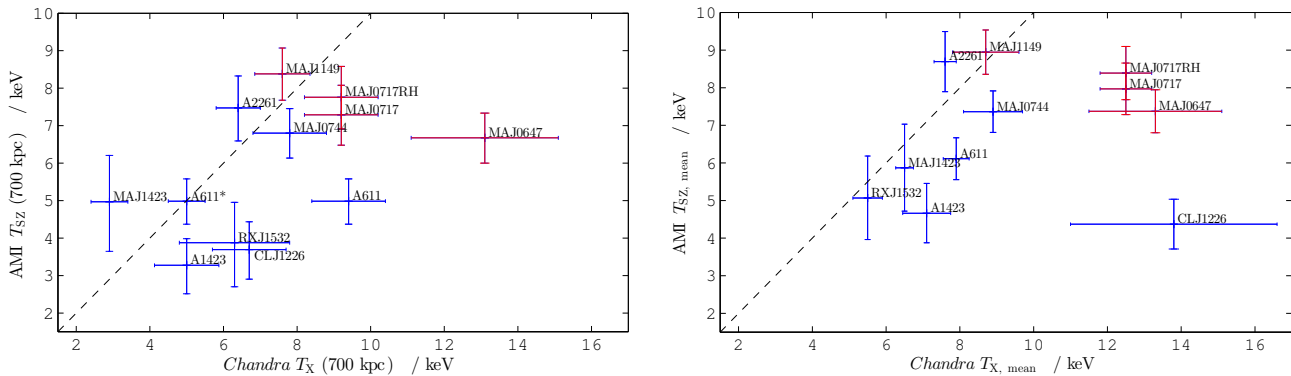
Figure 15. SZ and X-ray temperatures for each cluster: Left (a) Shows AMI SZ temperatures at $r = 700$ kpc plotted against X-ray annularly averaged temperatures at $r = 700$ kpc from the ACCEPT database. Right (b) Shows mean AMI SZ temperatures plotted against X-ray mean temperatures from Postman et al. (2012), both found in the range $(0.15 < r < 1)r_{500}$. Strong-lensing-selected sample members are displayed in red. Overplotted is the line of $T_{SZ} = T_X$. Error bars are 1σ.

are reported in the *Chandra* ACCEPT database[4] (Cavagnolo et al. 2009) in circular annuli which cover radii out to typically 500 to 1000 kpc. We calculate SZ temperatures at the highest radius that is reached by the *Chandra* temperature profiles of all 10 AMI-CLASH clusters, $r \approx 700$ kpc, to obtain comparable temperature estimates at radii at which we can constrain parameters with SZ data. We plot T_{SZ} versus T_X, at 700 kpc in Figure 15 (a). The ACCEPT temperature profile for A611 appears particularly uncertain, due to the automated way in which the analysis was carried out, necessitated by the size of this very useful database. A more detailed analysis of the same A611 *Chandra* data is available in Donnarumma et al. (2011) producing a much lower temperature at high radius with smaller errors. Both 700-kpc X-ray temperature estimates are included in Figure 15 (a).

Estimates of the *average* X-ray temperature are found from Chandra data in Maughan et al. (2008) (in the range $(0.15 < r < 1)r_{500}$) and Postman et al. (2012) (in the range 71.4 kpc – 714 kpc from the centre of each cluster). There is good agreement between Maughan et al. and Postman et al. on the temperatures of 5 of the 8 clusters in both samples. There are larger differences between CLJ1226+3332, MAJ0647+7015 and MAJ0717+3745 X-ray temperatures but these are still consistent given the quoted error estimates. We plot the mean AMI SZ temperature with the average cluster temperatures from Postman et al. in Figure 15(b). Comparing AMI SZ parameter values with three independent X-ray analyses addresses possible uncertainty regarding reduction and analysis methods. Figures 14 and 15 (b) highlight the same two populations of clusters within our sample. Figure 15 (a) is less demonstrative due to problems with annular averaging at high radius – this is discussed further in Section 7.2.

7.1.1 XMM–Chandra T_X discrepancy

In previous studies, X-ray estimated parameter values (such as gas mass) found using *Chandra* data are often higher than those found from *XMM-Newton* data: the discrepancies have been attributed to differences in temperature estimates between the instruments (see e.g. Mahdavi et al. 2013). Schellenberger et al. (2015) find the discrepancy to be energy dependent, increasing with temperature to ≈ 29 per cent at 12 keV (Earth-frame). Donahue et al. (2014) use

Table 7. Differences between temperature estimates for pairs of clusters in our sample. T_X values are core-excluded temperature estimates internal to r_{500} from *Chandra* observation (Postman et al. 2012) and *XMM* observation (Baldi et al. 2012). Uncertainties in T_X estimates are the errors quoted in the respective papers; "difference" significances have been obtained using the quadrature formula.

Cluster	*Chandra*		*XMM*	
	T_X / keV	difference	T_X / keV	difference
MAJ0647+7015	13.3 ± 1.80	2.23σ	$9.30^{+0.45}_{-0.37}$	2.32σ
MAJ0744+3927	8.9 ± 0.80	1.68σ	8.14 ± 0.34	2.49σ
CLJ1226+3332	13.8 ± 2.80		$10.16^{+0.77}_{-0.73}$	

XMM and *Chandra* T_X profiles of the CLASH sample and find a radial dependence: at 100 kpc they find no systematic difference in *XMM* and *Chandra* temperatures, but towards 1 Mpc the discrepancy reaches ≈ 25 per cent.

We investigate the apparent separation of clusters into two populations in Figure 15 (b) to see if an energy-dependent bias of *Chandra* temperatures (from Postman et al. 2012) could be responsible. Baldi et al. (2012) find *XMM* temperatures (in the range $(0.15 < r < 1)r_{500}$) for a sample of clusters including MAJ0744+3927, CLJ1226+3332 and MAJ0647+7015. From Figure 15 (b) MAJ0647+7015 and CLJ1226+3332 have similar, very high, $T_{X, mean}$ values. MAJ0744+3927 has a similar $T_{SZ, mean}$ value to MAJ0647+7015 but a much lower $T_{X, mean}$. In Table 7 we find differences between the temperatures measured for pairs of clusters by each instrument. Given the error estimates quoted in Baldi et al. and Postman et al., we see that MAJ0647+7015 and CLJ1226+3332 *Chandra* temperature estimates are not significantly biased high relative to MAJ0744+3927 compared with estimates from *XMM*. We emphasise that our clusters with high rest-frame temperatures tend to be at high redshift so that their measured temperatures are lower.

Baldi et al. (2012) find the ≈ 29 per cent discrepancy in T_X induces ≈ 15 per cent discrepancy in the mass estimate towards 12 keV; this does not account for the nearly 50 per cent discrepancies in AMI and *Chandra* mass estimates in Figure 14.

7.2 Comparison with simulations

Internal cluster dynamics during merger activity have been investigated through simulations covering a wide variety of merger scen-

arios and individual systems, see e.g. ZuHone, Markevitch, & Johnson (2010), van Weeren et al. (2011), Brüggen, van Weeren & Röttgering (2012) and Molnar, Hearn, & Stadel (2012). We focus on the comprehensive work of Poole et al. (2006), which follows the cluster merger process for three merger mass ratios for each of three merger impact parameters (see also Ricker & Sarazin 2001, Ritchie & Thomas 2002 and Randall, Sarazin, & Ricker 2002). From example merger stages in the paper itself and the suite of simulation videos online, at http://visav.phys.uvic.ca/~babul/Merger_PaperI/, this study provides simulations of both the X-ray and the SZ signals, ideal for the focus of this paper, as well as the X-ray temperature, gas surface density and entropy. While these simulations include the effects of radiative cooling, star formation and minimal feedback from supernovae, Poole et al. (2006) make clear that they do not include factors such as feedback from AGN, magnetic fields, pressure due to cosmic rays, and conduction.

In the following, we compare the simulated X-ray morphology and temperature maps with real X-ray maps and temperature profiles on the *Chandra* ACCEPT database. For clusters that appear relaxed, or very close to relaxed, we class their dynamical state as $\gtrsim 5\,$Gyr since first pericentre (the first closest approach of the secondary cluster to the primary), as depicted by Poole et al.: we class A611, A1423, A2261 and MAJ1423+2404 in this way.

The X-ray morphologies of A611 and A1423 do not look similar to any of the simulated merger stages, with circular shapes and no visible concentrations of X-ray emission. Neither cluster is present in the Maughan et al. (2008) sample, so are not included in Figure 14, but do not show significantly higher T_X values relative to T_{SZ} in Figure 15.

A2261 appears in both Figures 14 and 15, also showing no significant difference in X-ray and SZ estimated parameter values. The X-ray morphology most closely resembles the Poole et al. simulations after 5 Gyr apart from an area of isolated substructure lying approximately 0.7 Mpc from the cluster centre (see e.g. Maughan et al.). Given the low X-ray temperature and agreement of SZ and X-ray parameter estimates, it could be the start of a very high mass-ratio merger, well before first pericentre.

MAJ1423+2404 also has a relaxed X-ray morphology and displays little discrepancy between X-ray-estimated and SZ-estimated Y_X vs M_{gas} in Figure 14 and T_{SZ} vs T_X in Figure 15, also supporting a relaxed classification.

RXJ1532+3021 is reportedly a very strong cool-core cluster, supporting a relaxed classification. Hlavacek-Larrondo et al. (2013) investigate the X-ray morphology using *XMM-Newton* and deep *Chandra* observations and reveal central substructure from substantial AGN activity and a cold front. The authors conclude that the origin of the cold front is either cool gas dragged out by the AGN outburst or turbulence from sloshing of the cool core induced by a minor merger. Figure 15 shows good agreement between T_{SZ} and T_X values but SZ- and X-ray-derived Y_X and M_{gas} values in Figure 14 are more discrepant. This supports the theory of a low-level merger proposed by Hlavacek-Larrondo et al. which may be old enough to no longer exhibit the higher temperatures associated with mergers.

Although CLJ1226+3332 is classed by Allen et al. (2008) and Postman et al. (2012) as relaxed given its X-ray morphology, differences in SZ and X-ray parameter values suggest otherwise. Figures 14 and 15 show large discrepancies between X-ray and SZ in Y_X and M_{gas} and in average temperature estimates. The average X-ray temperature and temperature profiles from *Chandra* on the ACCEPT database, and *XMM-Newton* in Maughan et al. (2007), show very high temperatures for the low mass of

CLJ1226+3332, suggesting an early-stage merger. In conjunction with its circular shape, slightly displaced X-ray peak brightness from the cluster centre and some substructure towards the south-west, CLJ1226+3332 is likely a recent, close to head-on, minor merger. Maughan et al. and Jee & Tyson (2009) also discuss the non-relaxed state of CLJ1226+3332. Jee & Tyson compare their weak-lensing mass reconstruction with the X-ray temperature map of Maughan et al.: they note the correlation of a high-temperature asymmetry with an area of low-luminosity substructure to the south-west of the cluster centre, concluding that the substructure has just passed through the primary cluster.

MAJ0647+7015 (strong-lensing selected) has high values of $T_{X,\,mean}$ and $T_X(700\,kpc)$, both of which are very discrepant from the SZ values in Figure 15. Figure 14 shows large differences also between SZ and X-ray Y_X and M_{gas} values. The X-ray morphology is non-circular with no central peak in X-ray surface brightness which, along with the high T_X values, indicate MAJ0647+7015 has recently undergone a close to head-on major merger.

MAJ0717+3745 has a complicated X-ray morphology that suggests multiple mergers: a triple merger, according to Mann & Ebeling (2012). Figure 14 shows large differences between X-ray and SZ measurements of Y_X and M_{gas}. No significant discrepancy is evident between the SZ and X-ray temperatures at 700 kpc, in Figure 15. This is likely due to effects of annular averaging over a complex X-ray temperature distribution that is poorly approximated by the model profile in both X-ray and SZ analyses. This is supported by a larger discrepancy in average temperature, for which annular averaging was not used.

Parameter estimation for MAJ0744+3927 suggests a relaxed state. Both $T_{X,\,mean}$ and $T_X(700\,kpc)$ are consistent with the values estimated from SZ, shown by Figure 15, and there is no significant discrepancy in Y_X and M_{gas} between SZ and X-ray in Figure 14. The ACCEPT X-ray temperature profile shows a low peak temperature for the mass of the cluster and some evidence for a cool-core. However, the X-ray morphology does not appear relaxed: there is a clear displacement in X-ray peak brightness from the centre and some extended clump features. These indicate an old merger returning to a relaxed state, supported by the small cool core.

In a strong-lensing investigation of MAJ1149+2223, Smith et al. (2009) found the mass distribution to be best described as a main dark matter halo plus three, group-sized halos. Mann & Ebeling (2012) suggest that the high velocity dispersion, measured by Ebeling et al. (2007), arises from merging along the line of sight. There is, however, no significant discrepancy between X-ray–estimated and SZ–estimated parameter values in Figures 14 and 15; we argue that there are two reasons that may explain this. The first reason concerns the mass of the main halo compared with any of the masses of the group halos. Given the findings of Smith et al. and the low X-ray temperature, we expect the individual merging groups to be of low mass relative to the primary cluster: Poole et al. (2006) show the X-ray temperatures reached in binary mergers of 1:1 and 3:1 are much higher than in 10:1 mergers, where the temperature is lower with larger impact parameter. The lack of a high X-ray surface-brightness region in the ACCEPT *Chandra* maps also indicates that mergers are of high impact-parameter. The second reason concerns the complex shape of the system, evident in the ACCEPT images, for which annular averaging will be problematic. We expect the X-ray temperature profile to be biased low due to cooler, higher-radius gas being included in each annulus.

8 CONCLUSIONS

We have observed the eleven clusters in the CLASH sample that are accessible to AMI, and discard one due to a very bright source on the edge of the field of view. The remaining ten clusters have been analysed in a fully Bayesian way to give estimated parameter values from SZ measurement.

(i) Although 20 out of the 25 CLASH sample members were selected to be relaxed, we find disagreement in the literature on the dynamical states of many of our AMI-CLASH sub-sample, illustrating the difficulty in determining cluster dynamical state and identifying mergers.

(ii) We investigate the correlations in our model and use it to calculate $Y-M$ curves, varying $f_{\mathrm{gas},r_{200}}$ and redshift. We discuss the effect these parameters have on the power-laws fitted to the curves: $Y-M$ is dependent on the cluster redshift and on the value of $f_{\mathrm{gas},r_{200}}$.

(iii) X-ray studies have found sensitivity of the scatter about scaling relations to the dynamical states of the clusters included. Here, we investigate the sensitivity of our model correlations to dynamical state by introducing variations in cluster pressure profile shape parameters: a consequence of merger activity that can be induced in the analysis. In our analysis these are fixed to the "universal" values. Varying a, the shape parameter best constrained by AMI SZ data, over a large range induces only small changes in scaling relation power-laws. This is consistent with Poole et al. (2007) who track cluster observables of merging systems in the plane of scaling relations, finding very little perpendicular scatter but large variations along the scaling relation, over the course of a merger.

(iv) Due to the difference in dependence of SZ and X-ray measurement on n_{e}, X-ray observables are much more sensitive to changes in mass, pressure, temperature and density during a merger. Discrepancies between parameter estimates derived from SZ and X-ray measurement can help identify clusters undergoing mergers. Denoting $M_{\mathrm{gas}}T$ by Y_{X} (for X-ray and SZ), we compare two $Y_{\mathrm{X}}-M_{\mathrm{gas}}$ scaling relations of the sub-sample members: one plotted using AMI SZ parameter values and the second using *Chandra* X-ray parameters from Maughan et al. (2008). In addition to a difference in scatter we see an apparent "movement" of sample members along the line of the relation, between SZ and X-ray. These discrepancies are visualised by plotting the ratios of AMI and *Chandra* Y_{X} and M_{gas} values showing a population of our sub-sample for which the SZ and X-ray parameters agree well. Other clusters are discrepant by up to $\times 2$, all towards higher X-ray Y_{X} and M_{gas} values *along* the line of the relation.

(v) We also plot temperature estimates made from SZ and X-ray observation and find a similar split of clusters into two populations that are in agreement with those found from the ratios of AMI and *Chandra* Y_{X} and M_{gas} values. This result comes from the comparison of AMI SZ parameter estimates with those from three independent X-ray analyses, addressing possible inconsistencies between methods.

(vi) Dynamical state classifications in the literature of the ten clusters report: A611, MAJ1423+2404 and RXJ1532+3021 are relaxed; MAJ0647+7015, MAJ0717+3745 and MAJ1149+2223 are mergers; and A1423, A2261, CLJ1226+3332, and MAJ0744+3927 have mixed reports. Using discrepancies in SZ and X-ray parameter estimates and comparisons of Poole et al. (2006) merger simulations with X-ray morphology we determine the dynamical states of the ten clusters in the sub-sample. We class A611, A1423, A2261 and MAJ1423+2404 as relaxed. MAJ0647+7015 and MAJ0717+3745, selected for their lensing strength, we find

to be mergers. As expected from the mixed classifications in the literature, MAJ0744+3927 and CLJ1226+3332, although selected as relaxed, are also mergers. MAJ1149+2223, although reported in the literature as highly disturbed, shows no significant discrepancies between SZ and X-ray parameters. We conclude that low mass infalling cluster groups with high impact-parameters will cause less gas shocking and/or fractionation than lower mass-ratio mergers. We find evidence supporting the presence of an old, low level merger in RXJ1532+3021, postulated by Hlavacek-Larrondo et al. (2013).

References

Allen S. W., Schmidt R. W., Ebeling H., Fabian A. C., van Speybroeck L., 2004, MNRAS, 353, 457

Allen S. W., Rapetti D. A., Schmidt R. W., Ebeling H., Morris R. G., Fabian A. C., 2008, MNRAS, 383, 879

Andersson K., et al., 2011, ApJ, 738, 48

Arnaud M., Pointecouteau E., Pratt G. W., 2007, A&A, 474, L37

Arnaud M., Pratt G. W., Piffaretti R., Böhringer H., Croston J. H., Pointecouteau E., 2010, A&A, 517, A92

Baldi A., Ettori S., Molendi S., Gastaldello F., 2012, A&A, 545, A41

Bauer F. E., Fabian A. C., Sanders J. S., Allen S. W., Johnstone R. M., 2005, MNRAS, 359, 1481

Brüggen M., van Weeren R. J. & Röttgering H. J. A., 2012, MNRAS, 425, L76

Cavagnolo K. W., Donahue M., Voit G. M., Sun M., 2009, ApJS, 182, 12

Donahue M., et al., 2014, ApJ, 794, 136

Donnarumma A., et al., 2011, A&A, 528, A73

Ebeling H., Barrett E., Donovan D., Ma C.-J., Edge A. C., van Speybroeck L., 2007, ApJ, 661, L33

Feretti L., Giovannini G., Govoni F., Murgia M., 2012, A&ARv, 20, 54

Feroz F., Hobson M. P., 2008, MNRAS, 384, 449

Feroz F., Hobson M. P., Bridges M., 2009, MNRAS, 398, 1601

Feroz F., Hobson M. P., Zwart J. T. L., Saunders R. D. E., Grainge K. J. B., 2009, MNRAS, 398, 2049

Feroz F., Hobson M. P., Cameron E., Pettitt A. N., 2013, arXiv, arXiv:1306.2144

Franzen T. M. O., Davies, M. L., Waldram E. M., Grainge K. J. B., et al., 2011, MNRAS, 415, 2699

Gilmour R., Best P., Almaini O., 2009, MNRAS, 392, 1509

Giodini S., Lovisari L., Pointecouteau E., Ettori S., Reiprich T. H., Hoekstra H., 2013, SSRv, 177, 247

Handley W. J., Hobson M. P., Lasenby A. N., 2015, MNRAS, 450, L61

Handley W. J., Hobson M. P., Lasenby A. N., 2015, arXiv, arXiv:1506.00171

Hashimoto Y., Böhringer H., Henry J. P., Hasinger G., Szokoly G., 2007, A&A, 467, 485

Hlavacek-Larrondo J., et al., 2013, ApJ, 777, 163

Isobe T., Feigelson E. D., Akritas M. G., Babu G. J., 1990, ApJ, 364, 104

Jee M. J., Tyson J. A., 2009, ApJ, 691, 1337

Kaiser N., 1986, MNRAS, 222, 323

Komatsu E., et al., 2011, ApJS, 192, 18

Kravtsov A. V., Vikhlinin A., Nagai D., 2006, ApJ, 650, 128

Landry D., Bonamente M., Giles P., Maughan B., Joy M., Murray S., 2013, MNRAS, 433, 2790

Limousin M., et al., 2010, MNRAS, 405, 777

Mahdavi A., Hoekstra H., Babul A., Bildfell C., Jeltema T., Henry J. P., 2013, ApJ, 767, 116

Mann A. W., Ebeling H., 2012, MNRAS, 420, 2120

Maughan B. J., Jones L. R., Ebeling H., Scharf C., 2004, MNRAS, 351, 1193

Maughan B. J., Jones C., Jones L. R., Van Speybroeck L., 2007, ApJ, 659, 1125

Maughan B. J., Jones C., Forman W., Van Speybroeck L., 2008, ApJS, 174, 117

Medezinski E., et al., 2013, ApJ, 777, 43

Molnar S. M., Hearn N. C., Stadel J. G., 2012, ApJ, 748, 45

Motl P. M., Hallman E. J., Burns J. O., Norman M. L., 2005, ApJ, 623, L63

Nagai D., Kravtsov A. V., Vikhlinin A., 2007, ApJ, 668, 1

Navarro J. F., Frenk C. S., White S. D. M., 1997, ApJ, 490, 493

Neto A. F., et al., 2007, MNRAS, 381, 1450

Olamaie M., Hobson M. P., Grainge K. J. B., 2012, MNRAS, 423, 1534

Olamaie M., Hobson M. P., Grainge K. J. B., 2013, MNRAS, 430, 1344

Perley R. A., Butler B. J., 2013, ApJS, 204, 19

Planck Collaboration, et al. II, 2013, A&A, 550, A128

Planck Collaboration, et al. V, 2013, A&A, 550, A131

Poole G. B., Fardal M. A., Babul A., McCarthy I. G., Quinn T., Wadsley J., 2006, MNRAS, 373, 881

Poole G. B., Babul A., McCarthy I. G., Fardal M. A., Bildfell C. J., Quinn T., Mahdavi A., 2007, MNRAS, 380, 437

Postman M., et al., 2012, ApJS, 199, 25

Pratt G. W., Arnaud M., Pointecouteau E., 2006, A&A, 446, 429

Pratt G. W., Croston J. H., Arnaud M., Böhringer H., 2009, A&A, 498, 361

Randall S. W., Sarazin C. L., Ricker P. M., 2002, ApJ, 577, 579

Redlich M., Bartelmann M., Waizmann J.-C., Fedeli C., 2012, A&A, 547, A66

Ricker P. M., Sarazin C. L., 2001, ApJ, 561, 621

Ritchie B. W., Thomas P. A., 2002, MNRAS, 329, 675

Rodríguez-Gonzálvez C., Shimwell T. W., Davies M. L., Feroz F., et al., 2012, MNRAS, 425, 162

Rozo E., Vikhlinin A., More S., 2012, ApJ, 760, 67

Rozo E., Rykoff E. S., Bartlett J. G., Evrard A., 2014, MNRAS, 438, 49

Sayers J., et al., 2013, ApJ, 768, 177

Schammel M. P., et al., 2013, MNRAS, 431, 900

Schellenberger G., Reiprich T. H., Lovisari L., Nevalainen J., David L., 2015, A&A, 575, A30

Schmidt R. W., Allen S. W., 2007, MNRAS, 379, 209

Smith G. P., et al., 2009, ApJ, 707, L163

Sun M., Voit G. M., Donahue M., Jones C., Forman W., Vikhlinin A., 2009, ApJ, 693, 1142

Sunyaev R. A., Zel'dovich Y. B., 1972, CoASP, 4, 173

van Weeren R. J., Röttgering H. J. A., Brüggen M., Cohen A., 2009, A&A, 505, 991

van Weeren R. J., Brüggen M., Röttgering H. J. A., Hoeft M., 2011, MNRAS, 418, 230

Vikhlinin A., Kravtsov A., Forman W., Jones C., Markevitch M., Murray S. S., Van Speybroeck L., 2006, ApJ, 640, 691

Vikhlinin A., et al., 2009, ApJ, 692, 1033

Vikhlinin A., et al., 2009, ApJ, 692, 1060

Zhang Y.-Y., Finoguenov A., Böhringer H., Kneib J.-P., Smith G. P., Kneissl R., Okabe N., Dahle H., 2008, A&A, 482, 451

Zitrin A., et al., 2013, ApJ, 762, L30

ZuHone J. A., Markevitch M., Johnson R. E., 2010, ApJ, 717, 908

Zwart J. T. L., et al., 2008, MNRAS, 391, 1545

Zwart J. T. L., et al., 2011, MNRAS, 418, 2754